Aerospace Science and Technology 138 (2023) 108330

Contents lists available at ScienceDirect

Aerospace Science and Technology

journal homepage: www.elsevier.com/locate/aescte

Active optimization adjustment for the surface accuracy of spaceborne SAR antennas

Dewen Yu [a,b], Guobiao Hu [b,c], Saijie Cai [d], Yaowen Yang [b,*], Jun Hong [a,*]

[a] Key Laboratory of Modern Design and Rotor-Bearing System (Ministry of Education), School of Mechanical Engineering, Xi'an Jiaotong University, Xi'an 710049, China
[b] School of Civil and Environmental Engineering, Nanyang Technological University, Nanyang Avenue 639798, Singapore
[c] Thrust of Internet of Things, The Hong Kong University of Science and Technology (Guangzhou), Guangzhou 511400, China
[d] Key Laboratory of Thermo-Fluid Science and Engineering (Ministry of Education), School of Energy and Power Engineering, Xi'an Jiaotong University, Xi'an 710049, China

ARTICLE INFO

Article history:
Received 13 December 2022
Received in revised form 27 March 2023
Accepted 10 April 2023
Available online 17 April 2023
Communicated by Jae-Hung Han

Keywords:
Surface accuracy
Active adjustment
Thermoelastic deformation
Mixed-variable optimization
Spaceborne antenna

ABSTRACT

Inevitable disturbances in the spatial thermal environment will seriously degrade the surface accuracy of satellite antennas. Unfortunately, the ground pre-adjustment cannot adaptively guarantee the antenna performance under alternating thermal loadings. To tackle the challenge, this study proposes an active optimization adjustment method to achieve the required surface accuracy for spaceborne antennas. Starting from the comprehensive analysis of external thermal fluxes in outer space, the heat transfer model is firstly established to acquire the temperature field of the antenna system. Subsequently, considering the thermoelastic effect and the geometrical nonlinearity, the antenna surface accuracy is predicted. In particular, the thermoelastic forces induced from temperature changes and dimensional deviations are precisely determined by the absolute nodal coordinate formulation. Moreover, an efficient computational method with invariant matrices is developed to accelerate the prediction. On this basis, we construct the on-orbit active adjustment model to compensate for the effect of thermally induced deformation on the surface accuracy. A mixed-variable optimization algorithm is further put forward to find the optimal strategy of dimensional adjustment. Finally, a case study with simulation analysis and experiment verification demonstrates the feasibility and superiority of the proposed surface adjustment method.

1. Introduction

The spaceborne synthetic aperture radar (SAR), with unique advantages of spatial resolution and weather adaptability, has revolutionized remote sensing, satellite communication, and earth observation [1,2]. As mission-oriented challenges continue evolving, it is imperative to further upgrade the integrated performance of the SAR system. Physically, the Ruze formula [3] indicates that the gain of the main lobe directly depends on the antenna surface accuracy. Under this background, the surface root-mean-square (RMS) deviation is of a harsh requirement for achieving satisfactory performance [4]. Taking the antenna operating at the Ku-band as an example, the desired RMS deviation is only 0.33-0.50 mm [5]. However, the spaceborne antenna is inevitably exposed to extreme heat loads, and the thermally induced deformation will seriously deteriorate the surface accuracy [6]. Hence, how to actively conduct the deformation adjustment and adaptively optimize the surface accuracy of the antenna has been a great concern of practitioners [7].

In the past decade, several studies have explored mechanical compensation strategies to reduce the surface deviation of antennas. According to the technical feasibility, the current methods are based on either ground pre-adjustment or on-orbit active adjustment. Du et al. [8] presented an assembly adjustment strategy based on the propagation relationship between the surface deviation of the mesh reflector and the dimension variation of cables. To minimize the overall distortions of the mesh antenna, Xun et al. [9] established a fast

---

[*] Corresponding authors.
E-mail addresses: cywyang@ntu.edu.sg (Y. Yang), jhong@mail.xjtu.edu.cn (J. Hong).

https://doi.org/10.1016/j.ast.2023.108330
1270-9638/

predictive control algorithm with the electromechanical coupled dynamic model. Zhao et al. [10] developed a link adjustment approach to simultaneously optimize the surface accuracy and deployment reliability. Yu et al. [11] put forward a novel assembly accuracy control method for the SAR antenna, which allows to find the sparse adjustment combination with the same deviation. However, all these ground pre-adjustment strategies ignored the influence of thermally induced deformation on the antenna structures. In fact, since the spaceborne antenna periodically travels through the sunlight and shadow regions, the time-dependent thermal loads are the main cause of surface accuracy degradation [12,13]. Furthermore, the determined pre-adjustment under specific conditions cannot adaptively compensate for the surface accuracy in the ever-changing thermal environment [14].

To overcome the deficiencies of ground adjustment, the active adjustment strategies are investigated for the orbiting antennas. Wang et al. [15] and Song et al. [16] incorporated piezoelectric actuators into the cables of mesh reflectors for the on-orbit shape control. In addition, the electromechanical materials and shape memory alloys are also promising for regulating antenna deformation [17]. Inspired by the pioneering works of Padula et al. [18] and Liu and Hollaway [19], Zhang et al. [20–22] conducted integrated structural-electromagnetic optimization for the shape control of mesh reflectors. The radiation pattern degradation induced by random structural errors was quantified with enhanced iteration efficiency. Tanaka et al. [23] estimated the surface deformation from the changes in antenna gains, and further developed a correction method based on the sensitivity matrix. Although this method reduces the calculation cost compared to the traditional pseudo-inverse method [24,25], it demands adequate measurement of antenna deformations, restricting its application to on-orbit adjustment [26]. Lu et al. [27] proposed an on-orbit mechanical compensation method for the planar phased array antenna. However, the interaction between the support trusses and antenna panels was not considered, and the control performance was weakened. Treating the temperature distribution in the spaceborne antenna as an interval variable, Yang et al. [28] put forward an active adjustment method by incorporating the min-max concept with the incremental equilibrium equation. Considering the thermal effect and truss deformation, Nie et al. [29] optimized the structural parameters for mesh reflector antennas, which could also be transferred into the active shape adjustment. However, the above studies are built on the assumption that the temperature distribution is uniform throughout the antenna, whereas the on-orbit temperature field is actually uneven [30,31]. As to the surface accuracy compensation of spaceborne SAR antennas, the method accounting for the spatial-temporal characteristics of the temperature field has not been reported yet.

As can be seen from the above introduction, the premise of thermal-structural analysis for the spaceborne antenna is to determine the external thermal loadings and evaluate the temperature distribution [32]. The most commonly used approaches for thermal analysis are the thermal network method (TNM) and the finite element method (FEM) [33,34]. The TNM is suitable for simple thermal problems without complicated boundary conditions [35], and it needs to correct the selected parameters [36]. In contrast, FEM adopts interpolation functions to integrate the geometric model into the thermal analysis, making it more feasible to solve the temperature field of complex structures [37]. For example, Maksimov et al. [38] constructed FE-based theoretical formulas to quantify the thermal effect on a microstrip antenna. The FE software was employed to determine the transient temperature distribution of the AstroMesh antenna in [39]. Yu et al. [40] constructed the dynamic heat conduction equation for an on-orbit antenna subjected to time-variant thermal excitation. Although these numerical or theoretical models provide thermal information for key components such as beams or plates, it remains to systematically discuss the temperature field of the entire antenna, including the deployable support structure and the reflector panels.

As reviewed above, the existing shape control techniques are not feasible for the active adjustment of on-orbit antennas. Furthermore, none of the previous studies have comprehensively revealed the thermal-structural coupling effect on the surface accuracy. To fill these gaps, this research proposes an on-orbit optimization adjustment method to achieve the required performance for spaceborne SAR antennas. The surface accuracy prediction model that incorporates the thermoelastic effect with the geometrical nonlinearity is firstly constructed to determine the structural deformation in the service environment. Considering the prescribed constraints, the active shape adjustment problem is further transferred into a mixed-variable optimization problem. Afterward, an enhanced particle swarm optimization (PSO) algorithm is proposed to effectively minimize the on-orbit surface deviation.

The main contributions of this work are threefold. (1) Distinguished from previous studies that only conducted the shape control at ambient temperature, a comprehensive method is proposed to actively adjust the surface accuracy of on-orbit antennas, breaking through the limitation of the ground pre-adjustment. (2) Compared with the preceding thermal-structural analysis for antennas, the uneven temperature field at different orbital positions can be theoretically calculated, discarding the unrealistic assumption on the temperature distribution. (3) Taking advantage of the hybrid encoding scheme, an enhanced PSO algorithm for tackling the mixed-variable optimization problem is developed with an adaptive parameter tuning approach, which shows competitive performance in determining the adjustment strategy.

This article is structured as follows. To start with, the antenna structure and the focused problem are elaborated in Section 2. After quantifying the thermal fluxes in outer space, Section 3 derives the heat condition model for acquiring the temperature distribution. Section 4 formulates the thermoelastic deformation of the antenna system and proposes the surface accuracy prediction model. Subsequently, an enhanced PSO algorithm is developed to optimize the surface accuracy in Section 5. For demonstrating the validity of the proposed surface accuracy adjustment method, a case study is provided with numerical simulation and experimental verification in Section 6. Finally, Section 7 summarizes the concluding remarks.

2. Problem elaboration

As depicted in Fig. 1, the spaceborne SAR antenna to be investigated in this study, which belongs to the active phased-array antenna (APAA) type, consists of the load module, support links, and antenna panels. Apart from enhancing the structural stiffness, the support links also undertake the mission of surface accuracy adjustment. With resorting to embedded actuators such as PZT, the length of links can be changed to conduct the active shape adjustment for the antennal panels. After all, when the SAR satellite enters outer space, the surface accuracy degradation is inevitable because of thermally induced deformation.

It has been indicated that the surface accuracy directly affects the satellite imagery resolution. To be more specific, the surface accuracy refers to the deviation between the desired working surface and the actual reflector of antenna panels, which can be evaluated with different indicators, such as flatness, pose error, maximum deformation, and RMS deviation. After considering practical engineering advancements and deformation distribution characteristics [41,42], the RMS deviation is chosen as the metric to assess the surface accuracy

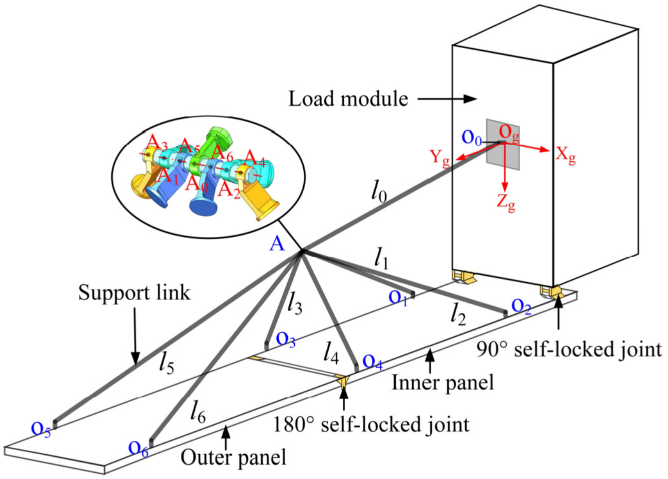

Fig. 1. Structure of the spaceborne SAR antenna.

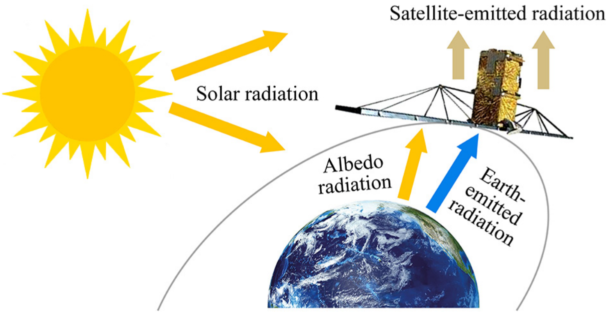

Fig. 2. Spatial heat fluxes and thermal conduction of an orbiting SAR satellite.

of antenna panels in this study. Assuming that there are n sample points, the RMS deviation Γ in the global coordinate system O_g-$X_gY_gZ_g$ is defined as

$$\Gamma = \sqrt{\frac{1}{n}\sum_{i=1}^{n}\left(\Delta x_i^2 + \Delta y_i^2 + \Delta z_i^2\right)} = \sqrt{\frac{1}{n}\sum_{i=1}^{n}\left(\mathbf{w}_i^{\mathrm{T}}\mathbf{w}_i\right)}, \tag{1}$$

where $\mathbf{w}_i = [\Delta x_i, \Delta y_i, \Delta z_i]^{\mathrm{T}}$ is the position deviation of each point along the three coordinate axes.

Under this background, our study focuses on optimizing the on-orbit surface accuracy by link adjustment. Aimed to minimize the RMS deviation, the optimization requires finding the proper position vector and the corresponding adjustment vector, which are discrete and continuous variables, respectively. Therefore, the problem actually belongs to a mixed-variable optimization problem.

To conduct the active optimization adjustment, three significant challenges must be tackled: (1) How to determine the temperature field of the on-orbit antenna with complex boundary conditions under the action of spatial heat fluxes? (2) How to construct the thermal-structural coupling model for the whole overconstrained system to achieve the surface accuracy prediction? (3) How to develop an effective mixed-variable optimization algorithm for finding the superb combination of dimensional adjustment? In what follows, our efforts will be devoted to breaking through those barriers.

3. Thermal analysis and heat transmission

When a satellite enters the predetermined orbit, the antenna panels inevitably suffer from solar radiation, Earth-emitted radiation, and Earth-reflected radiation. To reveal the impact of the spatial thermal environment on the antenna panel, this section will characterize these external heat fluxes and construct the thermal transmission model.

3.1. Quantification of heat fluxes in space

As illustrated in Fig. 2, the spaceborne antenna travels periodically from the shadow region to the sunshine zone, and its absorbed solar radiation flux q_s is formulated as

$$q_s = \alpha_p S_s f_s \cos\theta_s, \tag{2}$$

where the solar heat flux S_s is at an average of 1353 W/m^2 [37]; α_p is the solar absorptivity; the view factor f_s [30] depends on the antenna attitude; θ_s denotes the incident angle of sunlight.

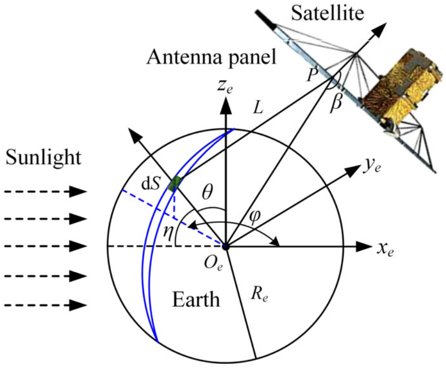

Fig. 3. Calculation of the Earth-reflected radiation flux.

When the sunlight strikes the Earth, part of it enters the atmosphere, while the rest bounces back into space. The Earth-reflected radiation also affects the low-orbit satellite, and the corresponding heat flux q_f received by the antenna is determined as

$$q_f = \alpha_p S_s \alpha_b \int\limits_{\varphi} \int\limits_{\theta} \frac{\cos\psi_{31}\cos\psi_{32}\cos\psi_{33}}{\pi L^2} R_e^2 \sin\theta \mathrm{d}\theta \mathrm{d}\varphi, \tag{3}$$

where the albedo factor α_b is about 0.35 [39], and the radius R_e of the Earth is 6371 km. As shown in Fig. 3, the spherical coordinate system (φ, θ) is constructed to describe the earth surface, and the distance L is calculated as

$$L = \sqrt{R_e^2 + (R_e + H_a)^2 - 2R_e(R_e + H_a)\cos\theta}, \tag{4}$$

where H_a is the orbital height of the satellite. Particularly, ψ_{31}, ψ_{32} and ψ_{33} [43] are given by

$$\begin{cases} \cos\psi_{31} = \begin{cases} \cos\theta\cos\phi + \sin\theta\sin\phi\cos\phi, & 0 \le \eta \le \pi/2 \\ 0, \quad \pi/2 < \eta \le \pi \end{cases} \\ \cos\psi_{32} = \begin{cases} \dfrac{R_e + H_a}{L}\cos\theta - \dfrac{R_e}{L}, & 0 \le \alpha_1 \le \pi/2 \\ 0, \quad \pi/2 < \alpha_1 \le \pi \end{cases} \\ \cos\psi_{33} = \begin{cases} \dfrac{1}{L}\left[(R_e + H_a - R_e\cos\theta)\cos\beta + \dfrac{R_e}{R_e + H_a}\sin\theta\sin\beta\cos\phi\right], & 0 \le \alpha_2 \le \pi/2 \\ 0, \quad \pi/2 < \alpha_2 \le \pi \end{cases} \end{cases}. \tag{5}$$

Analogous to the solar radiation, the Earth also emits radiation with the heat flux S_e of 237 W/m^2 [40]. As illustrated in Fig. 3, the absorbed Earth-emitted radiation flux q_e for the spaceborne antenna is expressed as

$$q_e = \frac{\alpha_e S_e}{\pi} \int\limits_{\varphi} \int\limits_{\theta} (\cos\theta\cos\beta + \sin\theta\sin\beta\cos\varphi)\sin\theta \mathrm{d}\theta \mathrm{d}\varphi. \tag{6}$$

where α_e is the absorptivity ratio, and β denotes the angle between the line connecting the Earth with the antenna and the inner normal of the panels.

Except for these external heat sources, the exothermic antenna also transfers thermal energy into outer space. Based on the Stefan-Boltzmann law, the radiation flux q_r is described as

$$q_r = \varsigma_p \sigma (T_s^4 - T_c^4), \tag{7}$$

where ς_p denotes the antenna emissivity, and σ represents the Boltzmann constant. In addition, T_s and T_c denote the structural and ambient temperatures, respectively.

3.2. Analytical model of thermal transmission

Since outer space is almost a vacuum that prevents thermal convection, the heat is only transferred by radiation and conduction. The three thermal boundary conditions in the spaceborne satellite are illustrated as

$$\begin{cases} \mathcal{B}_1 : T(x, y, z) = T_0 \\ \mathcal{B}_2 : k_x \dfrac{\partial T}{\partial x} n_x + k_y \dfrac{\partial T}{\partial y} n_y + k_z \dfrac{\partial T}{\partial z} n_z = q_0 \\ \mathcal{B}_3 : k_x \dfrac{\partial T}{\partial x} n_x + k_y \dfrac{\partial T}{\partial y} n_y + k_z \dfrac{\partial T}{\partial z} n_z = \varsigma_s \sigma (T^4 - T_c^4) \end{cases}, \tag{8}$$

where T is the temperature field; T_0 and q_0 are the initial temperature and the heat flux density of the boundary, respectively; k_x, k_y and k_z denote the thermal conductivities along the three coordinate axes, respectively; n_x, n_y and n_z correspond to the directional cosines of the unit normal vector.

For the support links, the temperature field is governed by

$$k_s A_s \frac{\partial^2 T}{\partial x^2} - \varsigma_s \sigma P_s \left(T^4 - T_c^4\right) + (q_s + q_f + q_e + q_r) D_s \cos\gamma_s = \rho_s c_s A_s \frac{\partial T}{\partial t}, \tag{9}$$

where k_s, ς_s, and c_s denote the axial conductivity, surface emissivity, and specific heat of links, respectively; ρ_s is the material density; P_s, D_s, and A_s represent the perimeter, diameter, and cross-section area, respectively; γ_s denotes the angle between the panel and the corresponding link. When the temperature field achieves a steady state, it yields $\partial T/\partial t = 0$. According to the variational principle, the solution of Eq. (9) makes the following function at its minimum:

$$I_s = \int\limits_l \left[\frac{1}{2} k_s A_s \left(\frac{\partial T}{\partial x}\right)^2 + \frac{1}{5} \varsigma_s \sigma P_s T^5 - (q_s + q_f + q_e + q_r) D_s T + \rho_s c_s A_s \frac{\partial T}{\partial t} T\right] \mathrm{d}l. \tag{10}$$

Subsequently, the support links are divided into finite thermal elements with two nodes $[T_i,\ T_j]$, and the linear interpolation [27] is applied to construct the temperature distribution inside each element. As suggested by [44,45], $T^4 = 4T_0^3 T - 3T_0^4$ is employed to eliminate the fourth-order term. On this basis, the thermal balance equation of each support link is formulated as

$$(\mathbf{K}_1^e + \mathbf{K}_2^e)\mathbf{q}_T^e = \mathbf{Q}_l^e, \tag{11}$$

where the thermal transfer matrices are expressed as

$$\begin{aligned} &\mathbf{K}_1^e = \frac{k_s A}{l^e} \begin{bmatrix} 1 & -1 \\ -1 & 1 \end{bmatrix}, \qquad \mathbf{K}_2^e = \frac{2}{3} \varsigma_s \sigma P_s l^e T_r^3 \begin{bmatrix} 2 & 1 \\ 1 & 2 \end{bmatrix}, \\ &\mathbf{Q}_l^e = \frac{1}{2} P_s (q_s + q_f + q_e + q_r) l^e \begin{bmatrix} 1 \\ 1 \end{bmatrix} + \frac{3}{2} \varsigma_s \sigma P_s l^e T_0^4 \begin{bmatrix} 1 \\ 1 \end{bmatrix}. \end{aligned} \tag{12}$$

Furthermore, by combining Fourier's theorem with the latter two thermal boundary conditions, one can also obtain the temperature field of antenna panels by minimizing the function:

$$\begin{aligned} I_p = {} & \frac{1}{2} \int\limits_{\Omega_p} \left[k_1 \left(\frac{\partial T}{\partial x}\right)^2 + k_2 \left(\frac{\partial T}{\partial y}\right)^2 + k_3 \left(\frac{\partial T}{\partial z}\right)^2 - 2\rho_p T \left(Q_p - c_p \frac{\partial T}{\partial t}\right)\right] \mathrm{d}\Omega \\ & - \int\limits_{S_p} \varsigma_p \sigma \left(\frac{1}{5} T^5 - T T_c^4\right) \mathrm{d}S - \int\limits_{S_p} T\,(q_l + q_u)\,\mathrm{d}S \end{aligned}, \tag{13}$$

where k_1, k_2, and k_3 are the thermal conductivities of panels along the three coordinate axes, respectively; ρ_p and c_p are the material density and the specific heat of panels, respectively; Q_p is the strength of internal heat source; q_l and q_u denote the total thermal fluxes of the lower and upper surfaces, respectively; S_p and Ω_p are the surface area and the volume of panels, respectively;

According to the FEM, the temperature distribution of antenna panels can be characterized by the shape function $\mathbf{N}_p$ and the nodal temperature vector $\mathbf{q}_T^e$ as below:

$$T(x, y, z) = \mathbf{N}_p(x, y, z)\mathbf{q}_T^e. \tag{14}$$

By uniting Eqs. (13)-(14), the governing equation for the steady-state thermal transfer is derived as

$$\mathbf{K}_T^e \mathbf{q}_T^e = \mathbf{Q}_T^e, \tag{15}$$

where the element matrices are determined by

$$\begin{cases} \mathbf{K}_T^e = \displaystyle\int\limits_{\Omega^e} \left[k_1 \left(\frac{\partial \mathbf{N}}{\partial x}\right)^{\mathrm{T}} \left(\frac{\partial \mathbf{N}}{\partial x}\right) + k_2 \left(\frac{\partial \mathbf{N}}{\partial y}\right)^{\mathrm{T}} \left(\frac{\partial \mathbf{N}}{\partial y}\right) + k_3 \left(\frac{\partial \mathbf{N}}{\partial z}\right)^{\mathrm{T}} \left(\frac{\partial \mathbf{N}}{\partial z}\right)\right] \mathrm{d}\Omega \\ \mathbf{Q}_T^e = \displaystyle\int\limits_{\Omega^e} \rho_a Q_a \mathbf{N}^{\mathrm{T}} \mathrm{d}\Omega + \int\limits_{S_a^e} q_u \mathbf{N}^{\mathrm{T}} \mathrm{d}S + \int\limits_{S_a^e} q_l \mathbf{N}^{\mathrm{T}} \mathrm{d}S + \int\limits_{S_a^e} \varsigma_p \sigma_p T_c^4 \mathbf{N}^{\mathrm{T}} \mathrm{d}S \end{cases}. \tag{16}$$

Within the standard finite element framework, the matrices and nodal vectors are assembled to establish the heat transfer equation for the whole system, which takes the form as

$$\mathbf{K}_T \mathbf{q}_T = \mathbf{Q}_T \tag{17}$$

where $\mathbf{K}_T$ is associated with $\mathbf{K}_1^e$, $\mathbf{K}_2^e$ and $\mathbf{K}_T^e$; $\mathbf{q}_T$ is composed of all nodal temperatures; $\mathbf{Q}_T$ depends on $\mathbf{Q}_l^e$ and $\mathbf{Q}_T^e$. According to the above formulation, the overall temperature field can be completely determined by the Newton-Raphson algorithm [46].

4. Surface accuracy prediction for the spaceborne antenna

After determining the temperature field of the spaceborne antenna, we will further develop the thermal-elastic coupling model with the absolute nodal coordinate formulation (ANCF). Considering the high nonlinearity that exists in the deformation analysis, an improved computational strategy will also be proposed to calculate the thermoelastic force efficiently in this section.

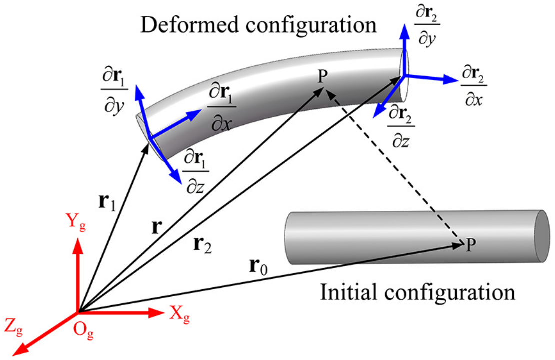

Fig. 4. Two-node beam element with the ANCF.

4.1. Thermoelastic deformation of support links

For comprehensively capturing the deformation of support links, it is suggested to utilize the ANCF beam element to describe the structural flexibility [47,48]. Unlike the conventional finite element method based upon the infinitesimal rotation assumption, the ANCF directly adopts position gradients instead of rotation angles to guarantee the continuity of the strain field [49]. As a milestone in the development history of flexible multibody modeling, the ANCF method offers many advantages, including but not limited to, an exact geometric description [50], a global representation [48], the capability of increasing the interpolation order without increasing the number of nodes [51], and the ability to solve linear or nonlinear strain-displacement relationships [52,53]. Given these advantages, the ANCF has been widely applied to model aerospace structures [30,48,54]. Herein, a thermal integrated beam element with the ANCF is developed to reveal the coupled thermoelastic behavior of support links.

Since previous researches [27,47] have demonstrated that beam elements are more suitable than link elements in characterizing support links, the ANCF beam element with a complete gradient rather than a deficient gradient is adopted in this study. As shown in Fig. 4, the structural deformation of the ANCF beam element is directly characterized and evaluated in the global frame. The arbitrary coordinate vector $\mathbf{r}$ is formulated as

$$\mathbf{r}=\mathbf{S}(x,y,z)\,\mathbf{e}=\mathbf{S}(x,y,z)\left[\mathbf{r}_1^{\mathrm{T}},\left(\frac{\partial \mathbf{r}_1}{\partial x}\right)^{\mathrm{T}},\left(\frac{\partial \mathbf{r}_1}{\partial y}\right)^{\mathrm{T}},\left(\frac{\partial \mathbf{r}_1}{\partial z}\right)^{\mathrm{T}},\mathbf{r}_2^{\mathrm{T}},\left(\frac{\partial \mathbf{r}_2}{\partial x}\right)^{\mathrm{T}},\left(\frac{\partial \mathbf{r}_2}{\partial y}\right)^{\mathrm{T}},\left(\frac{\partial \mathbf{r}_2}{\partial z}\right)^{\mathrm{T}}\right]^{\mathrm{T}}, \tag{18}$$

in which the shape function matrix $\mathbf{S}$ [55] is associated with the local coordinates x, y and z. For the beam element, its generalized external force $\mathbf{Q}_b$ can be induced from the principle of virtual work, which is given by

$$\mathbf{Q}_b=\mathbf{S}^{\mathrm{T}}(x,y,z)\,\mathbf{F}_0, \tag{19}$$

where $\mathbf{F}_0$ denotes the original external force vector.

From the perspective of continuum mechanics, the deformation gradient matrix $\mathbf{J}$ of the beam element is a function of the derivative of the position vector:

$$\mathbf{J}=\frac{\partial \mathbf{r}}{\partial \mathbf{x}}\left(\frac{\partial \mathbf{r}_0}{\partial \mathbf{x}}\right)^{-1}=\begin{bmatrix}\frac{\partial \mathbf{S}}{\partial x}\mathbf{e} & \frac{\partial \mathbf{S}}{\partial y}\mathbf{e} & \frac{\partial \mathbf{S}}{\partial z}\mathbf{e}\end{bmatrix}^{\mathrm{T}}\mathbf{J}_0^{-1}, \tag{20}$$

where the global coordinate vector $\mathbf{r}_0$ is defined in the initial configuration, and $\mathbf{x}$ denotes the local coordinate vector. Accordingly, the Green-Lagrange strain tensor $\boldsymbol{\varepsilon}_m$ can be calculated by

$$\boldsymbol{\varepsilon}_m=\frac{1}{2}(\mathbf{J}^{\mathrm{T}}\mathbf{J}-\mathbf{I})=\frac{1}{2}\begin{bmatrix}\mathbf{e}^{\mathrm{T}}\mathbf{S}_a\mathbf{e}-1 & \mathbf{e}^{\mathrm{T}}\mathbf{S}_d\mathbf{e} & \mathbf{e}^{\mathrm{T}}\mathbf{S}_f\mathbf{e}\\ & \mathbf{e}^{\mathrm{T}}\mathbf{S}_b\mathbf{e}-1 & \mathbf{e}^{\mathrm{T}}\mathbf{S}_e\mathbf{e}\\ sym & & \mathbf{e}^{\mathrm{T}}\mathbf{S}_c\mathbf{e}-1\end{bmatrix}. \tag{21}$$

More intuitively, the symmetric property allows the tensor $\boldsymbol{\varepsilon}_m$ to be recast into a compact vector form:

$$\boldsymbol{\varepsilon}_b^0=[\varepsilon_{11},\varepsilon_{22},\varepsilon_{33},2\varepsilon_{12},2\varepsilon_{13},2\varepsilon_{23}]^{\mathrm{T}}, \tag{22}$$

where ε_{ij} is the (i,j)-th component of $\boldsymbol{\varepsilon}_m$. Considering the thermal expansion effect, the above strain vector is modified as

$$\boldsymbol{\varepsilon}_b=[\varepsilon_{11}-\Delta T_s\varpi_s,\varepsilon_{22},\varepsilon_{33},2\varepsilon_{12},2\varepsilon_{13},2\varepsilon_{23}]^{\mathrm{T}}, \tag{23}$$

where ΔT_s denotes the corresponding temperature difference along the axes of support links, and ϖ_s denotes the thermal expansion coefficient.

According to the constitutive relationship between the strain and stress tensors, the strain energy U of the ANCF beam element is expressed as

$$
\begin{aligned}
U &= \frac{1}{2}\int\limits_{V} \boldsymbol{\varepsilon}_b^{\mathrm{T}}\mathbf{E}_b\boldsymbol{\varepsilon}_b \mathrm{d}V \\
&= \int \left[\frac{\lambda+2\mu}{2}\left(\varepsilon_{11}^2+\varepsilon_{22}^2+\varepsilon_{33}^2\right)+2\mu\left(\varepsilon_{12}^2+\varepsilon_{13}^2+\varepsilon_{23}^2\right)+\lambda\left(\varepsilon_{11}\varepsilon_{22}+\varepsilon_{11}\varepsilon_{33}+\varepsilon_{22}\varepsilon_{33}\right)\right]\mathrm{d}V+, \\
&\int\left[\frac{\lambda+2\mu}{2}\left(\Delta T_s\varpi_s\right)^2-\lambda\Delta T_s\varpi_s\left(\varepsilon_{11}+\varepsilon_{22}+\varepsilon_{33}\right)-2\mu\Delta T_s\varpi_s\varepsilon_{11}\right]\mathrm{d}V
\end{aligned}
\tag{24}
$$

where the elasticity matrix $\mathbf{E}_b$ depends on Lame constants λ and μ. By differentiating Eq. (24) with respect to $\mathbf{e}$, the mapping from the nodal deformation and the thermoelastic force $\mathbf{Q}$ is constructed as follows:

$$
\mathbf{Q}=\frac{\partial U}{\partial \mathbf{e}}=\mathbf{K}_b(\mathbf{e},\Delta T_b)\mathbf{e}. \tag{25}
$$

Notice that the stiffness matrix $\mathbf{K}_b$ not only requires the volume integrals of large matrices, but also varies with the nodal coordinates and temperature distributions. What is worse, multiple iterations are generally inevitable for solving and optimizing the displacement field. If the elastic force is directly calculated via the above formula, the computation process will be very tedious and time-consuming due to the high nonlinearity and strong coupling. To tackle this problem, an improved solving strategy will be proposed to isolate the nodal coordinates and temperature variables from the numerical integration.

For calculating the elastic force efficiently and accurately, the whole stiffness matrix $\mathbf{K}_b$ is firstly decomposed into the following three parts:

$$
\mathbf{K}_b(\mathbf{e},\Delta T_s)=\mathbf{K}_1+\mathbf{K}_2\Delta T_s+\mathbf{K}_3(\mathbf{e}), \tag{26}
$$

where the matrices $\mathbf{K}_1$, $\mathbf{K}_2$ and $\mathbf{K}_3$ are formulated as

$$
\begin{cases}
\mathbf{K}_1=-\dfrac{3\lambda+2\mu}{2}\displaystyle\int\limits_V\left(\mathbf{S}_a+\mathbf{S}_b+\mathbf{S}_c\right)\mathrm{d}V \\
\mathbf{K}_2=-\lambda\varpi_s\displaystyle\int\limits_V\left(\mathbf{S}_a+\mathbf{S}_b+\mathbf{S}_c\right)\mathrm{d}V-2\mu\varpi_s\int\limits_V\mathbf{S}_a\mathrm{d}V \\
\mathbf{K}_3=\dfrac{\lambda+2\mu}{2}\displaystyle\int\limits_V\left(\mathbf{S}_a\mathbf{e}\mathbf{e}^{\mathrm{T}}\mathbf{S}_a+\mathbf{S}_b\mathbf{e}\mathbf{e}^{\mathrm{T}}\mathbf{S}_b+\mathbf{S}_c\mathbf{e}\mathbf{e}^{\mathrm{T}}\mathbf{S}_c\right)\mathrm{d}V+ \\
\dfrac{\lambda}{2}\displaystyle\int\limits_V\left(\mathbf{S}_a\mathbf{e}\mathbf{e}^{\mathrm{T}}\mathbf{S}_b+\mathbf{S}_a\mathbf{e}\mathbf{e}^{\mathrm{T}}\mathbf{S}_c+\mathbf{S}_b\mathbf{e}\mathbf{e}^{\mathrm{T}}\mathbf{S}_a+\mathbf{S}_b\mathbf{e}\mathbf{e}^{\mathrm{T}}\mathbf{S}_c+\mathbf{S}_c\mathbf{e}\mathbf{e}^{\mathrm{T}}\mathbf{S}_a+\mathbf{S}_c\mathbf{e}\mathbf{e}^{\mathrm{T}}\mathbf{S}_b\right)\mathrm{d}V+ \\
\mu\displaystyle\int\limits_V\left[\left(\mathbf{S}_d+\mathbf{S}_d^{\mathrm{T}}\right)\mathbf{e}\mathbf{e}^{\mathrm{T}}\mathbf{S}_d+\left(\mathbf{S}_e+\mathbf{S}_e^{\mathrm{T}}\right)\mathbf{e}\mathbf{e}^{\mathrm{T}}\mathbf{S}_e^{\mathrm{T}}+\left(\mathbf{S}_f+\mathbf{S}_f^{\mathrm{T}}\right)\mathbf{e}\mathbf{e}^{\mathrm{T}}\mathbf{S}_f\right]\mathrm{d}V
\end{cases}. \tag{27}
$$

Obviously, $\mathbf{K}_1$ and $\mathbf{K}_2$ are constant because $\mathbf{S}_a$, $\mathbf{S}_b$, $\mathbf{S}_c$, $\mathbf{S}_d$, $\mathbf{S}_e$ and $\mathbf{S}_f$ are fully determined in the initial configuration. For the coordinate-dependent matrix $\mathbf{K}_3$, we further reconstruct its (i,j)-th component into the quadric form as below:

$$
\left[\mathbf{K}_3(\mathbf{e})\right]_{ij}=\mathbf{e}^{\mathrm{T}}\mathbf{G}_{\mathbf{K}}^{ij}\mathbf{e}, \tag{28}
$$

where $\mathbf{G}_{\mathbf{K}}^{ij}$ is given by

$$
\begin{aligned}
\mathbf{G}_{\mathbf{K}}^{ij}=&\frac{\lambda+2\mu}{2}\int\limits_V\left[(\mathbf{S}_a)_i^{\mathrm{T}}\left(\mathbf{S}_a^{\mathrm{T}}\right)_j+(\mathbf{S}_b)_i^{\mathrm{T}}\left(\mathbf{S}_b^{\mathrm{T}}\right)_j+(\mathbf{S}_c)_i^{\mathrm{T}}\left(\mathbf{S}_c^{\mathrm{T}}\right)_j\right]\mathrm{d}V+ \\
&\frac{\lambda}{2}\int\limits_V\left[(\mathbf{S}_a)_i^{\mathrm{T}}\left(\mathbf{S}_b^{\mathrm{T}}\right)_j+(\mathbf{S}_a)_i^{\mathrm{T}}\left(\mathbf{S}_c^{\mathrm{T}}\right)_j+(\mathbf{S}_b)_i^{\mathrm{T}}\left(\mathbf{S}_a^{\mathrm{T}}\right)_j+(\mathbf{S}_b)_i^{\mathrm{T}}\left(\mathbf{S}_c^{\mathrm{T}}\right)_j+(\mathbf{S}_c)_i^{\mathrm{T}}\left(\mathbf{S}_a^{\mathrm{T}}\right)_j+(\mathbf{S}_c)_i^{\mathrm{T}}\left(\mathbf{S}_b^{\mathrm{T}}\right)_j\right]\mathrm{d}V+. \\
&\frac{\mu}{2}\int\limits_V\left[\left(\mathbf{S}_d+\mathbf{S}_d^{\mathrm{T}}\right)_i^{\mathrm{T}}\left(\mathbf{S}_d^{\mathrm{T}}\right)_j+\left(\mathbf{S}_e+\mathbf{S}_e^{\mathrm{T}}\right)_i^{\mathrm{T}}\left(\mathbf{S}_e^{\mathrm{T}}\right)_j+\left(\mathbf{S}_f+\mathbf{S}_f^{\mathrm{T}}\right)_i^{\mathrm{T}}\left(\mathbf{S}_f^{\mathrm{T}}\right)_j\right]\mathrm{d}V
\end{aligned}
\tag{29}
$$

It is pointed out that $\mathbf{G}_{\mathbf{K}}^{ij}$ is also an invariant matrix that can be directly invoked after initialization. Consequently, the improved formula successfully transforms the complex calculation into simple matrix multiplications. Moreover, the symmetry of $\mathbf{K}_3$ $(\mathbf{e})$ indicates that only the invariant matrices corresponding to the upper triangle and diagonal components of $\mathbf{K}_3$ need to be calculated.

As formulated above, both the nodal coordinate vector $\mathbf{e}$ and the temperature difference ΔT_s are completely eliminated from the volume integrals. By storing the invariant matrices $\mathbf{K}_1$, $\mathbf{K}_2$ and $\mathbf{G}_{\mathbf{K}}^{ij}$ in advance, only simple mathematical manipulation is required instead of repeated integration operations. In addition, one can readily determine the Jacobian matrix of the thermoelastic force without resorting to numerical operations, because the same invariant matrices appear in its exact analytical solution:

$$
\left(\frac{\partial \mathbf{Q}}{\partial \mathbf{e}}\right)_{ik}=\frac{\partial \mathbf{Q}_i}{\partial \mathbf{e}_k}=\left(\mathbf{K}_1+\mathbf{K}_2\Delta T_s\right)_{ik}+\sum_{j=1}^{24}\sum_{s=1}^{24}\mathbf{e}_s\left[\mathbf{G}_{\mathbf{K}_3}^{ij}+\left(\mathbf{G}_{\mathbf{K}_3}^{ij}\right)^{\mathrm{T}}\right]_{sk}\mathbf{e}_j. \tag{30}
$$

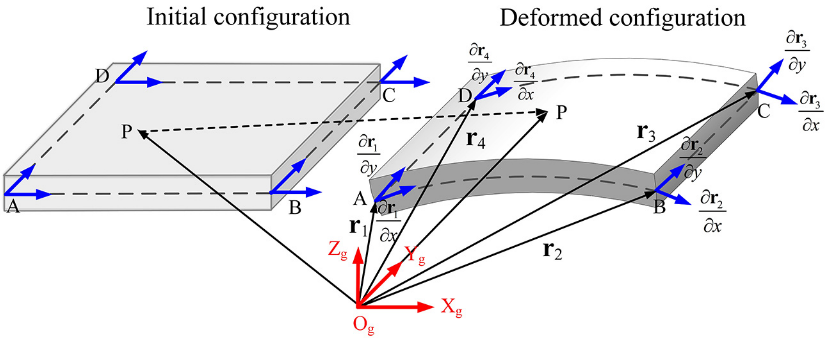

Fig. 5. ANCF thin plate element with four nodes.

Therefore, the developed computational strategy can significantly improve the solving efficiency of thermoelastic deformation for the support links.

4.2. Thermoelastic deformation of antenna panels

Since the thickness-width ratio is less than 0.1, the thin plate element is suitable for describing the thermoelasticity of antenna panels. In order to release the assumptions on the deformation of the cross section in the traditional incremental FEM [56], the ANCF is still applied to precisely construct the displacement field of plate elements. On this basis, the corresponding computational strategy of the thermoelastic force and the Jacobian matrix is also developed for the plate element to improve the solving efficiency of the whole procedure.

Within the ANCF framework, the four-node thin plate element possesses 36 degrees of freedom. As depicted in Fig. 5, an arbitrary position vector $\mathbf{r}$ in the ANCF thin plate element is described as

$$\mathbf{r}=\mathbf{S}_p(x,y)\mathbf{e}=\mathbf{S}_p(x,y)\left[\mathbf{r}_1^{\mathrm{T}},\left(\frac{\partial \mathbf{r}_1}{\partial x}\right)^{\mathrm{T}},\left(\frac{\partial \mathbf{r}_1}{\partial y}\right)^{\mathrm{T}},\mathbf{r}_2^{\mathrm{T}},\left(\frac{\partial \mathbf{r}_2}{\partial x}\right)^{\mathrm{T}},\left(\frac{\partial \mathbf{r}_2}{\partial y}\right)^{\mathrm{T}},\mathbf{r}_3^{\mathrm{T}},\left(\frac{\partial \mathbf{r}_3}{\partial x}\right)^{\mathrm{T}},\left(\frac{\partial \mathbf{r}_3}{\partial y}\right)^{\mathrm{T}},\mathbf{r}_4^{\mathrm{T}},\left(\frac{\partial \mathbf{r}_4}{\partial x}\right)^{\mathrm{T}},\left(\frac{\partial \mathbf{r}_4}{\partial y}\right)^{\mathrm{T}}\right]^{\mathrm{T}}, \tag{31}$$

where the shape function $\mathbf{S}_p$ [57] is associated with the local coordinates x and y, while $\mathbf{r}_i$ $(i=1,2,3,4)$ is the global position vector. Similar to the ANCF beam element, the generalized external force $\mathbf{Q}_p$ for the plate element is determined by

$$\mathbf{Q}_p=\mathbf{S}_p^{\mathrm{T}}(x,y)\,\mathbf{F}_0. \tag{32}$$

It is known from the Kirchhoff plate theory [58] that two parts are involved with the strain energy of the plate element. The first part accounts for the normal and shear deformations, while the second part is induced by the bending and twisting effect. Given the constitutive matrices $\mathbf{E}_\varepsilon$ and $\mathbf{E}_\kappa$, the strain energy U can be calculated by

$$U=\frac{1}{2}\int\limits_V \boldsymbol{\varepsilon}^{\mathrm{T}}\mathbf{E}_\varepsilon\boldsymbol{\varepsilon}\,\mathrm{d}V+\frac{1}{2}\int\limits_V \boldsymbol{\kappa}^{\mathrm{T}}\mathbf{E}_\kappa\boldsymbol{\kappa}\,\mathrm{d}V. \tag{33}$$

The strain tensor $\boldsymbol{\varepsilon}$ after incorporating the thermal expansion effect is revised as

$$\boldsymbol{\varepsilon}=\left[\varepsilon_{xx},\varepsilon_{yy},2\varepsilon_{xy}\right]^{\mathrm{T}}=\left[\frac{1}{2}\left(\frac{\partial \mathbf{r}}{\partial x}\right)^{\mathrm{T}}\left(\frac{\partial \mathbf{r}}{\partial x}\right)-\frac{1}{2},\frac{1}{2}\left(\frac{\partial \mathbf{r}}{\partial y}\right)^{\mathrm{T}}\left(\frac{\partial \mathbf{r}}{\partial y}\right)-\frac{1}{2},\left(\frac{\partial \mathbf{r}}{\partial x}\right)^{\mathrm{T}}\left(\frac{\partial \mathbf{r}}{\partial y}\right)\right]^{\mathrm{T}}-\left[\Delta T_x\varpi_x,\Delta T_y\varpi_y,0\right]^{\mathrm{T}}, \tag{34}$$

where ΔT_x and ΔT_y denote the temperature differences along the x and y axes, respectively; ϖ_x and ϖ_y correspond to the thermal expansion coefficients of antenna panels in the two directions. Besides, the curvature $\boldsymbol{\kappa}$ is formulated as

$$\boldsymbol{\kappa}=\left[\kappa_{xx},\kappa_{yy},2\kappa_{xy}\right]^{\mathrm{T}}=\left[\frac{\left(\frac{\partial^2\mathbf{r}}{\partial x^2}\right)^{\mathrm{T}}\mathbf{n}}{\|\mathbf{n}\|^3},\frac{\left(\frac{\partial^2\mathbf{r}}{\partial y^2}\right)^{\mathrm{T}}\mathbf{n}}{\|\mathbf{n}\|^3},2\frac{\left(\frac{\partial^2\mathbf{r}}{\partial x\partial y}\right)^{\mathrm{T}}\mathbf{n}}{\|\mathbf{n}\|^3}\right]^{\mathrm{T}},\quad \mathbf{n}=\frac{\partial \mathbf{r}}{\partial x}\times\frac{\partial \mathbf{r}}{\partial y}. \tag{35}$$

As to the ANCF thin plate element, the generalized thermoelastic force $\mathbf{Q}_e$ is determined by

$$\mathbf{Q}_e=\frac{\partial U}{\partial \mathbf{e}}=\mathbf{Q}_\varepsilon+\mathbf{Q}_\kappa, \tag{36}$$

where the components $\mathbf{Q}_\varepsilon$ and $\mathbf{Q}_\kappa$ are written as

$$\begin{cases}\mathbf{Q}_\varepsilon=\int\limits_V \frac{E}{1-\nu^2}\left(\varepsilon_{xx}\frac{\partial\varepsilon_{xx}}{\partial \mathbf{e}}+\varepsilon_{yy}\frac{\partial\varepsilon_{yy}}{\partial \mathbf{e}}\right)+\frac{2E}{1+\nu}\varepsilon_{xy}\frac{\partial\varepsilon_{xy}}{\partial \mathbf{e}}+\frac{\nu E}{1-\nu^2}\left(\varepsilon_{xx}\frac{\partial\varepsilon_{yy}}{\partial \mathbf{e}}+\varepsilon_{yy}\frac{\partial\varepsilon_{xx}}{\partial \mathbf{e}}\right)\mathrm{d}V\\ \mathbf{Q}_\kappa=\int\limits_V \frac{Eh^3}{12\left(1-\nu^2\right)}\left(\kappa_{xx}\frac{\partial\kappa_{xx}}{\partial \mathbf{e}}+\kappa_{yy}\frac{\partial\kappa_{yy}}{\partial \mathbf{e}}\right)+\frac{Eh^3}{6\left(1+\nu\right)}\kappa_{xy}\frac{\partial\kappa_{xy}}{\partial \mathbf{e}}+\frac{\nu Eh^3}{12(1-\nu^2)}\left(\kappa_{xx}\frac{\partial\kappa_{yy}}{\partial \mathbf{e}}+\kappa_{yy}\frac{\partial\kappa_{xx}}{\partial \mathbf{e}}\right)\mathrm{d}V\end{cases}. \tag{37}$$

Here, h, E, and ν represent the thickness, Young's modulus, and Poisson's ratio of antenna panels, respectively. To be more specific, the partial derivatives of strain and curvature tensors are given by

$$\left\{\begin{aligned} \frac{\partial \varepsilon_{xx}}{\partial \mathbf{e}} &= \mathbf{S}_x^{\mathrm{T}}\mathbf{S}_x\mathbf{e} \\ \frac{\partial \varepsilon_{yy}}{\partial \mathbf{e}} &= \mathbf{S}_y^{\mathrm{T}}\mathbf{S}_y\mathbf{e} \\ \frac{\partial \varepsilon_{xy}}{\partial \mathbf{e}} &= \mathbf{S}_x^{\mathrm{T}}\mathbf{S}_y\mathbf{e} \end{aligned}\right. , \left\{\begin{aligned} \frac{\partial \kappa_{xx}}{\partial \mathbf{e}} &= \frac{1}{\|\mathbf{n}\|^3}\left[\left(\frac{\partial^3 \mathbf{r}}{\partial x^2 \partial \mathbf{e}}\right)^{\mathrm{T}}\mathbf{n} + \left(\frac{\partial \mathbf{n}}{\partial \mathbf{e}}\right)^{\mathrm{T}}\frac{\partial^2 \mathbf{r}}{\partial x^2}\right] - \frac{3}{\|\mathbf{n}\|^5}\left(\frac{\partial^2 \mathbf{r}}{\partial x^2}\right)^{\mathrm{T}}\mathbf{n}\left(\frac{\partial \mathbf{n}}{\partial \mathbf{e}}\right)^{\mathrm{T}}\mathbf{n} \\ \frac{\partial \kappa_{yy}}{\partial \mathbf{e}} &= \frac{1}{\|\mathbf{n}\|^3}\left[\left(\frac{\partial^3 \mathbf{r}}{\partial y^2 \partial \mathbf{e}}\right)^{\mathrm{T}}\mathbf{n} + \left(\frac{\partial \mathbf{n}}{\partial \mathbf{e}}\right)^{\mathrm{T}}\frac{\partial^2 \mathbf{r}}{\partial y^2}\right] - \frac{3}{\|\mathbf{n}\|^5}\left(\frac{\partial^2 \mathbf{r}}{\partial y^2}\right)^{\mathrm{T}}\mathbf{n}\left(\frac{\partial \mathbf{n}}{\partial \mathbf{e}}\right)^{\mathrm{T}}\mathbf{n} \\ \frac{\partial \kappa_{xy}}{\partial \mathbf{e}} &= \frac{1}{\|\mathbf{n}\|^3}\left[\left(\frac{\partial^3 \mathbf{r}}{\partial x \partial y \partial \mathbf{e}}\right)^{\mathrm{T}}\mathbf{n} + \left(\frac{\partial \mathbf{n}}{\partial \mathbf{e}}\right)^{\mathrm{T}}\frac{\partial^2 \mathbf{r}}{\partial x \partial y}\right] - \frac{3}{\|\mathbf{n}\|^5}\left(\frac{\partial^2 \mathbf{r}}{\partial x \partial y}\right)^{\mathrm{T}}\mathbf{n}\left(\frac{\partial \mathbf{n}}{\partial \mathbf{e}}\right)^{\mathrm{T}}\mathbf{n} \end{aligned}\right. , \tag{38}$$

where $\mathbf{S}_x$ and $\mathbf{S}_y$ are the derivatives of $\mathbf{S}_p$ with respect to x and y, respectively.

It can be found that high nonlinearity exists in the relation among the thermoelastic force, the nodal coordinates and the temperature differences. Considering that the direct numerical differentiation is neither efficient nor accurate, an enhanced computational strategy is further developed to solve the thermoelastic force and the corresponding Jacobian matrix for the plate element.

For recasting the expression of the thermoelastic force into the simple matrix multiplication, the following matrices are introduced for ease of representation:

$$\mathbf{M} = \mathbf{S}_x^{\mathrm{T}}\mathbf{S}_x, \mathbf{N} = \mathbf{S}_y^{\mathrm{T}}\mathbf{S}_y, \mathbf{H} = \mathbf{S}_x^{\mathrm{T}}\mathbf{S}_y. \tag{39}$$

Thereby, the partial derivatives of strain tensor can be evaluated by

$$\frac{\partial \varepsilon_{xx}}{\partial \mathbf{e}_i} = \sum_{k=1}^{36}\mathbf{M}_{ki}\mathbf{e}_k, \frac{\partial \varepsilon_{yy}}{\partial \mathbf{e}_i} = \sum_{k=1}^{36}\mathbf{N}_{ki}\mathbf{e}_k, \frac{\partial \varepsilon_{xy}}{\partial \mathbf{e}_i} = \frac{1}{2}\left(\sum_{k=1}^{36}\mathbf{H}_{ki}\mathbf{e}_k + \sum_{m=1}^{36}\mathbf{H}_{im}\mathbf{e}_m\right), \tag{40}$$

where $\mathbf{M}_{ki}$ refers to the (k, i)-th item of $\mathbf{M}$, and similar definitions are possessed by $\mathbf{N}_{ki}$ and $\mathbf{H}_{ki}$. Subsequently, the nodal coordinates and temperature differences are extracted from the volume integral. For the i-th elastic force $(\mathbf{Q}_\varepsilon)_i$ originated from normal and shear deformations, it can be reconstructed as

$$(\mathbf{Q}_\varepsilon)_i = \sum_{k=1}^{36}\sum_{m=1}^{36}\sum_{n=1}^{36}[(\mathbf{A}_1)_{ikmn} + (\mathbf{A}_2)_{ikmn} + (\mathbf{A}_3)_{ikmn}]\mathbf{e}_k\mathbf{e}_m\mathbf{e}_n - (1 + 2\Delta T_x\varpi_x)\sum_{j=1}^{36}(\mathbf{B}_1)_{ji}\mathbf{e}_j - (1 + 2\Delta T_y\varpi_y)\sum_{j=1}^{36}(\mathbf{B}_2)_{ji}\mathbf{e}_j. \tag{41}$$

Specifically, the invariant matrices are derived as

$$\left\{\begin{aligned} (\mathbf{A}_1)_{ikmn} &= \frac{E}{2(1-\nu^2)}\int_V (\mathbf{M}_{km}\mathbf{M}_{ni} + \mathbf{N}_{km}\mathbf{N}_{ni})\,\mathrm{d}V \\ (\mathbf{A}_2)_{ikmn} &= \frac{\nu E}{2(1-\nu^2)}\int_V (\mathbf{N}_{km}\mathbf{M}_{ni} + \mathbf{M}_{km}\mathbf{N}_{ni})\,\mathrm{d}V \\ (\mathbf{A}_3)_{ikmn} &= \frac{E}{2(1+\nu)}\int_V (\mathbf{H}_{km}\mathbf{H}_{in} + \mathbf{H}_{km}\mathbf{H}_{ni})\,\mathrm{d}V \\ (\mathbf{B}_1)_{ji} &= \frac{E}{2(1-\nu^2)}\int_V \left(\mathbf{M}_{ji} + \nu\mathbf{N}_{ji}\right)\mathrm{d}V \\ (\mathbf{B}_2)_{ji} &= \frac{E}{2(1-\nu^2)}\int_V \left(\mathbf{N}_{ji} + \nu\mathbf{M}_{ji}\right)\mathrm{d}V \end{aligned}\right. , \tag{42}$$

where $(\mathbf{A}_w)_{ikmn}$ $(w = 1, 2, 3)$ corresponds to the in the $(i, 1296k + 36m + n - 1332)$-th entity of $\mathbf{A}_w$, and $(\mathbf{B}_s)_{ji}$ $(s = 1, 2)$ denotes the (j, i)-th item of $\mathbf{B}_s$. It should be emphasized that $\mathbf{A}_1$, $\mathbf{A}_2$, $\mathbf{A}_3$, $\mathbf{B}_1$, and $\mathbf{B}_2$ are constant matrices, allowing to be calculated and stored in advance. As formulated above, the Jacobian matrix of $(\mathbf{Q}_\varepsilon)_i$ can be further derived with the same invariant matrices in an explicit form:

$$\begin{aligned} \frac{\partial (\mathbf{Q}_\varepsilon)_i}{\partial \mathbf{e}_j} = &\sum_{m=1}^{36}\sum_{n=1}^{36}\left[(\mathbf{A}_1)_{jmni} + (\mathbf{A}_2)_{jmni} + (\mathbf{A}_3)_{jmni} + 2(\mathbf{A}_1)_{imjn} + 2(\mathbf{A}_2)_{imjn} + (\mathbf{A}_3)_{imjn} + (\mathbf{A}_3)_{ijmn}\right]\mathbf{e}_m\mathbf{e}_n \\ &- \left[(1 + 2\Delta T_x\varpi_x)(\mathbf{B}_1)_{ji} + (1 + 2\Delta T_y\varpi_y)(\mathbf{B}_2)_{ji}\right] \end{aligned}. \tag{43}$$

In accordance with the procedure of $\mathbf{Q}_\varepsilon$, one can deduce the efficient calculation formula of the thermoelastic force $\mathbf{Q}_\kappa$ resulting from the bending and twisting. In summary, by introducing the invariant matrices and removing all variables from the integral, the proposed solving strategy not only facilitates the accurate calculation of thermoelastic force and its Jacobian matrix, but also significantly lightens the computational burden.

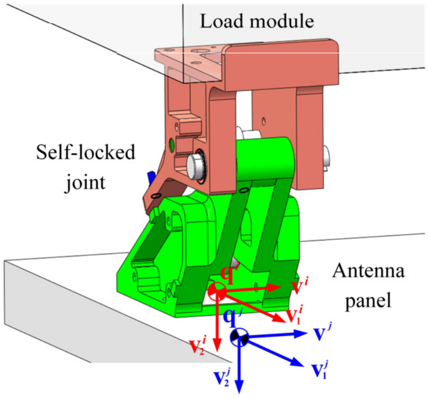

Fig. 6. Constraint formulation between the joint and the panel.

4.3. Determination of the surface accuracy

Like the assembly process of FEM, all the ANCF elements can be fully incorporated [49]. Besides, the Lagrange multiplier technique enables integrating the geometric constraint equations $\boldsymbol{\Phi}$ into the governing equation of the whole structure. Consequently, the thermoelastic deformation of the antenna system is summarized as

$$\begin{cases} \mathbf{Q}_w(\mathbf{q},\mathbf{q}_T) - \mathbf{Q}_f + \boldsymbol{\Phi}_{\mathbf{q}}^{\mathrm{T}}\boldsymbol{\lambda} = \mathbf{0} \\ \boldsymbol{\Phi}(\mathbf{q}) = \mathbf{0} \end{cases}, \tag{44}$$

where $\mathbf{q}$ consists of all nodal coordinate vectors, and λ denotes the Lagrange multiplier vector. $\mathbf{Q}_w$ and $\mathbf{Q}_f$ are the generalized matrices of thermoelastic force and external force, respectively. $\boldsymbol{\Phi}_{\mathbf{q}}$ denotes the Jacobian matrix of the constraint equation set. Note that the temperature differences ΔT_b, ΔT_x and ΔT_y are determined by the temperature vector as shown in Eq. (17), and thus $\mathbf{Q}_w$ is the function of both $\mathbf{q}$ and $\mathbf{q}_T$.

In particular, $\mathbf{Q}_f$ originates from the dimensional adjustment of support links. If the length of the i-th link is increased by Δl_i, the operation is equivalent to imposing an axial force $F_i = E_s A \Delta l_i / l_i$ [7], where E_s is the elastic modulus and l_i represents the design length of the i-th link. For description, the dimensional adjustment vector is defined as $\mathbf{a} = [\Delta l_1, \Delta l_2, \Delta l_3, \Delta l_4, \Delta l_5, \Delta l_6, \Delta l_7]^{\mathrm{T}}$, which directly determines $\mathbf{Q}_f$.

Without loss of generality, the geometric relationship between the self-locked joint and the antenna panel is elaborated to illustrate how to obtain the constraint equations $\boldsymbol{\Phi}$. As depicted in Fig. 6, the global position vectors $\mathbf{r}_P^i$ and $\mathbf{r}_P^j$ of the connection points $\mathbf{q}^i$ and $\mathbf{q}^j$, respectively, must coincide with each other. Moreover, along the joint axis, two unit direction vectors $\mathbf{v}^i$ and $\mathbf{v}^j$ can be defined for the self-locked joint and the antenna panel, respectively. These two vectors are always parallel to each other, i.e., $\mathbf{v}^i \times \mathbf{v}^j = 0$. Mathematically, the cross-product can be fully alternated by three independent dot-product equations. Hence, the constraint equations of the self-locked joint are formulated as

$$\boldsymbol{\Phi}(\mathbf{q}^i,\mathbf{q}^j) = \left[(\mathbf{r}_P^i - \mathbf{r}_P^j)^{\mathrm{T}} \quad (\mathbf{v}_1^i)^{\mathrm{T}}\mathbf{v}^j \quad (\mathbf{v}_2^i)^{\mathrm{T}}\mathbf{v}^j \quad (\mathbf{v}_1^i)^{\mathrm{T}}\mathbf{v}_2^j \right]^{\mathrm{T}} = \mathbf{0}, \tag{45}$$

where $\mathbf{v}_1^i$ and $\mathbf{v}_2^i$ are two orthogonal vectors perpendicular to $\mathbf{v}^i$, and $\mathbf{v}_2^j$ is similarly defined with respect to $\mathbf{v}^j$.

As formulated above, the Newton-Raphson iterative algorithm is also applied to obtain the nonlinear thermal-structural response. It is worth noting that the preceding sections have explicitly represented the thermoelastic force and the Jacobian matrix with invariant matrices. The proposed computational strategy not only avoids the repeated integral operation in Eq. (43), but also enables readily obtaining the correction value without tedious numerical differentiation during the iteration process. Therefore, the solving time of the displacement field is greatly shortened.

Under the interaction of the thermoelastic effect with the geometrical nonlinearity, once all nodal coordinates are determined, the position deviation $\mathbf{w}_i = [\Delta x_i, \Delta y_i, \Delta z_i]^{\mathrm{T}}$ can be extracted with the Boolean matrix $\mathbf{C}_i$, i.e., $\mathbf{w}_i = \mathbf{C}_i\mathbf{q}$. According to the definition of Eq. (1), it is easy to quantify the RMS deviation of the antenna. As such, the relation between the surface accuracy and the input parameters has been comprehensively revealed, which is represented as

$$\Gamma = f(\mathbf{a},\mathbf{g},\mathbf{h}), \tag{46}$$

where the input vectors $\mathbf{g}$ and $\mathbf{h}$ represent the intrinsic structure parameters and external heat fluxes, respectively.

5. Surface accuracy optimization for the spaceborne antenna

After developing the surface accuracy prediction model, this section will further propose an enhanced PSO algorithm for the active shape control of antenna panels. Taking the advantages of the evolutionary techniques, the classical PSO is endowed with novel hybrid encoding and reproduction schemes for solving the mixed-variable optimization problem. Moreover, an adaptive tuning approach is put forward to update the algorithm parameters for achieving robust optimization performance.

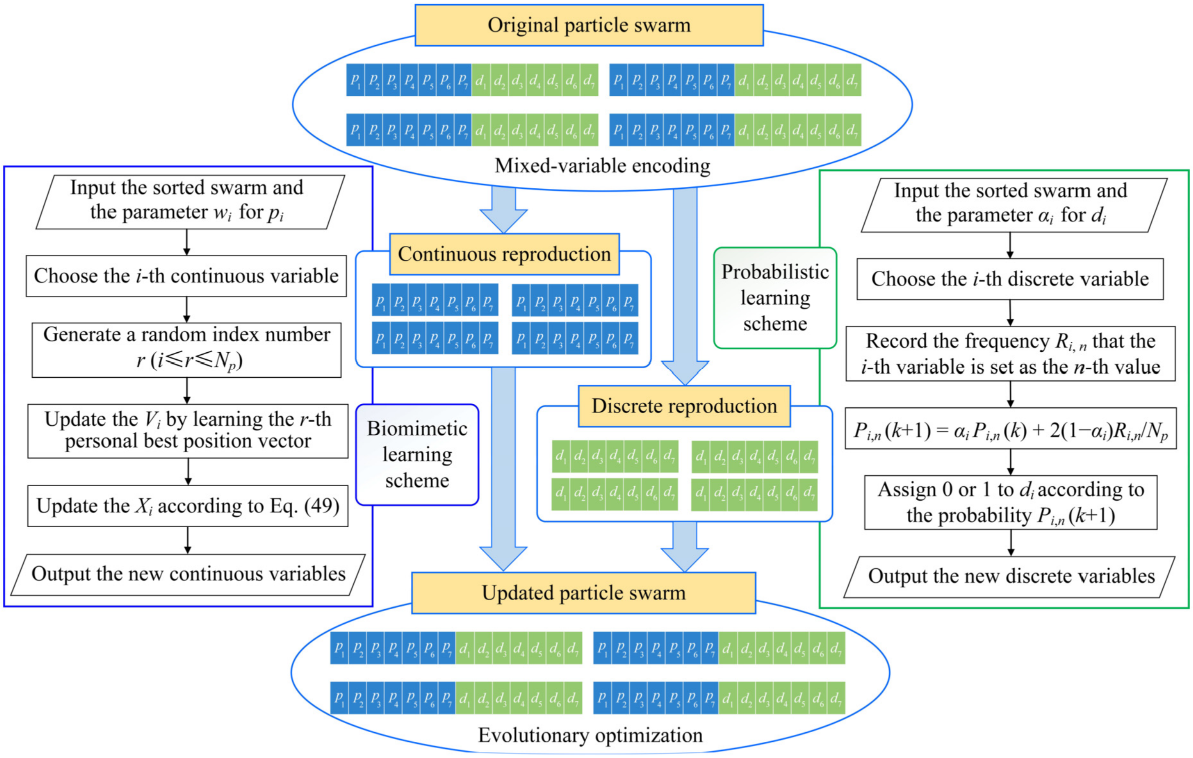

Fig. 7. Encoding and reproduction schemes for the mixed variables.

5.1. *Optimization model of the active surface adjustment*

Aimed to minimize the RMS deviation, the optimization requires finding the proper position vector **p** and the corresponding assignment vector **d**. Specifically speaking, $\mathbf{p} = [p_1, p_2, p_3, p_4, p_5, p_6, p_7]^{\mathrm{T}}$ is a Boolean vector where "1" indicates the link is to be adjusted. The assignment vector $\mathbf{d} = [d_1, d_2, d_3, d_4, d_5, d_6, d_7]^{\mathrm{T}}$ denotes the desired length variation on the condition that all links are adjustable. In this manner, the actual dimensional adjustment vector can be determined as $\mathbf{a} = \mathbf{p} * \mathbf{d}$, where $*$ represents the Hadamard product.

Besides, there are three practical constraints for the system. First, the maximum displacement of each point is restricted by the prescribed threshold $\mathbf{Z}_{\max}$. Secondly, to ensure structural reliability, the dimensional adjustment of links is confined within the interval $[d_{\min}, d_{\max}]$. Thirdly, considering the energy consumption of actuators, it is preferred to create a tradeoff between the attainable surface accuracy and the number of adjusted links, which means that an upper boundary n_a ($n_a \leq 7$) exists for the latter.

In summary, the optimization problem of the surface accuracy is formulated as

$$\begin{cases} \text{find} & \mathbf{p} = [p_1, p_2, p_3, p_4, p_5, p_6, p_7]^{\mathrm{T}} \\ & \mathbf{d} = [d_1, d_2, d_3, d_4, d_5, d_6, d_7]^{\mathrm{T}} \\ \min & \Gamma = \sqrt{\dfrac{1}{n}\displaystyle\sum_{i=1}^{n}\left(\mathbf{w}_i^{\mathrm{T}}\mathbf{w}_i\right)} = f\left(\mathbf{p}^{\mathrm{T}}\mathbf{d}, \mathbf{g}, \mathbf{h}\right) \\ \text{s.t.} & \mathbf{w}_i \leq \mathbf{w}_{\max} \\ & p_i = 0 \text{ or } p_i = 1 \quad (i = 1, 2, \cdots, 7) \\ & \displaystyle\sum_{i=1}^{7} p_i = n_a \\ & d_{\min} \leq d_i \leq d_{\max} \quad (i = 1, 2, \cdots, 7) \end{cases}, \tag{47}$$

Note that the vectors ***p*** and ***d*** are discrete and continuous variables, respectively. Therefore, the model belongs to a mixed-variable optimization problem.

5.2. *Hybrid encoding and reproduction schemes*

To overcome the defects of the pure relaxation or discretization method, hybrid operators are developed to tackle discrete and continuous variables separately. To accommodate the standard PSO framework [59], the position vector of each particle is encoded as $X_i = [p_1, p_2, \ldots, p_7, d_1, d_2, \ldots, d_7]$. For the first seven parameters that describe the combination of link adjustment, the probabilistic learning scheme is proposed to reproduce these discrete variables. For the remaining parameters that denote the dimensional adjustment values, the biomimetic learning scheme is developed to generate new continuous variables. The detailed process is described in Fig. 7.

Table 1
Structural parameters of the antenna system (Unit: mm).

Parameter	Symbol	Value	Parameter	Symbol	Value
Length of the auxiliary link	l_0	1026.41	Length of each antenna panel	l_p	1400.00
Length of the internal link	l_1, l_2	1081.26	Width of each antenna panel	w_p	834.50
Length of the middle link	l_3, l_4	630.14	Height of each antenna panel	h_p	20.00
Length of the external link	l_5, l_6	1288.10	Diameter of the support links	d	25.00

Drawing inspiration from the cooperative evolution, we make the update of discrete variables benefiting from the historical record of the whole swarm. To be more specific, the higher probability a discrete value appears in history, the more likely the corresponding variable will choose it. According to the basic criteria, the reproduction process for the discrete variables is designed as follows.

In the beginning, all values for these discrete binary variables are initialized with equal probability, i.e. $P_{i,n}(0) = 1/2$. Here, $P_{i,n}(k)$ denotes the probability that the i-th variable is set as the n-th candidate value in the k-th iteration. In the subsequent iterations, the dominant position vectors of the superior particles will be learned by new particles. To this end, we record the frequency $R_{i,n}$ that the i-th variable is assigned to the n-th value, and the assignment probability is updated by

$$P_{i,n}(k+1) = \alpha_i P_{i,n}(k) + 2(1-\alpha_i) R_{i,n}/N_p, \tag{48}$$

where α_i is the assignment coefficient, and N_p is the population of the particle swarm. It is highlighted that the first and second terms in the updating rule contain the historical and current search information, respectively. This combination seeks a trade-off between exploration and exploitation.

Compared with the operator of discrete variables, there are more variants of PSO for processing continuous variables. Most of these improved algorithms try to avoid premature by increasing the population diversity. However, fully random learning may deteriorate the convergence of the optimization algorithms. To strike the balance between warm diversity and convergence performance, the particles not only learn from the global record, but also draw on their own experience. As suggested by [60], the updating rules for the velocity V_i and the position X_i are modified as

$$\begin{cases} V_i(k+1) = w_v V_i(k) + 2c_r \left[P_{b,r}(k) - X_i(k) \right] \\ X_i(k+1) = X_i(k) + V_i(k+1) \end{cases}, \tag{49}$$

where $P_{b,r}(k)$ is randomly selected from the excellent personal positions of the k-th generation; w_v is the inertia weight, and the random number c_r is distributed in $[0, 1]$. For a complete explanation on the velocity and position of particles, interested readers can refer to [61,62].

As formulated above, the assignment coefficient α_i and the inertia weight w_v have a significant influence on the optimization performance. Moreover, it is inappropriate for all particles to set these parameters to fixed values. Hence, an adaptive parameter tuning strategy is developed to find suitable α_i and w_v for the PSO. The basic idea originates from incorporating historical search information to yield random parameters with good convergence. Specifically, the average values $\overline{\alpha}_i$ and $\overline{w}_v$ from historical optimal particles are initialized as 0.5. In each iteration, the two parameters will be generated by Student's T distribution or Gaussian distributions. The bell-shaped Gaussian distribution with a small variance will make the parameter approach its mean value, while the Student's T distribution has a fatter tail so that values with more diversity will be produced.

5.3. An enhanced PSO algorithm for the mixed-variable optimization

Taking the advantages of the penalty technique in simplicity and implementation [63], the inequality and equality constraints are transformed by adding the violation terms to the original fitness function. Finally, the enhanced PSO algorithm for the mixed-variable optimization is summarized in Fig. 8.

6. Case study

The proposed active optimization adjustment method will be demonstrated in this section. Firstly, the developed surface accuracy prediction model is examined by the experimental results at ambient temperature. On this basis, the on-orbit dimensional adjustment is implemented to optimize the antenna surface accuracy, and the analytical results show the superiority of the established methodology.

6.1. Introduction of structural and thermoelastic parameters

Taking a typical SAR antenna as an example, the active optimization adjustment is to be investigated to verify the technical feasibility. In compliance with the actual product configuration, the structural parameters of the antenna system are given in Table 1, and its thermoelastic characteristics are provided in Table 2. In practical engineering, the negative manufacturing tolerances are designed for all support links.

Considering the reliability of the antenna system, the allowable adjustment ranges for the auxiliary, internal, middle, and external links are [−3.08, 3.08] mm, [−3.24, 3.24] mm, [−1.89, 1.89] mm, and [−3.86, 3.86] mm, respectively. In addition, the antenna demands that the RMS deviation of two panels should be better than 2 mm, and the maximum deformation in the antenna panels is required to be less than 18 mm.

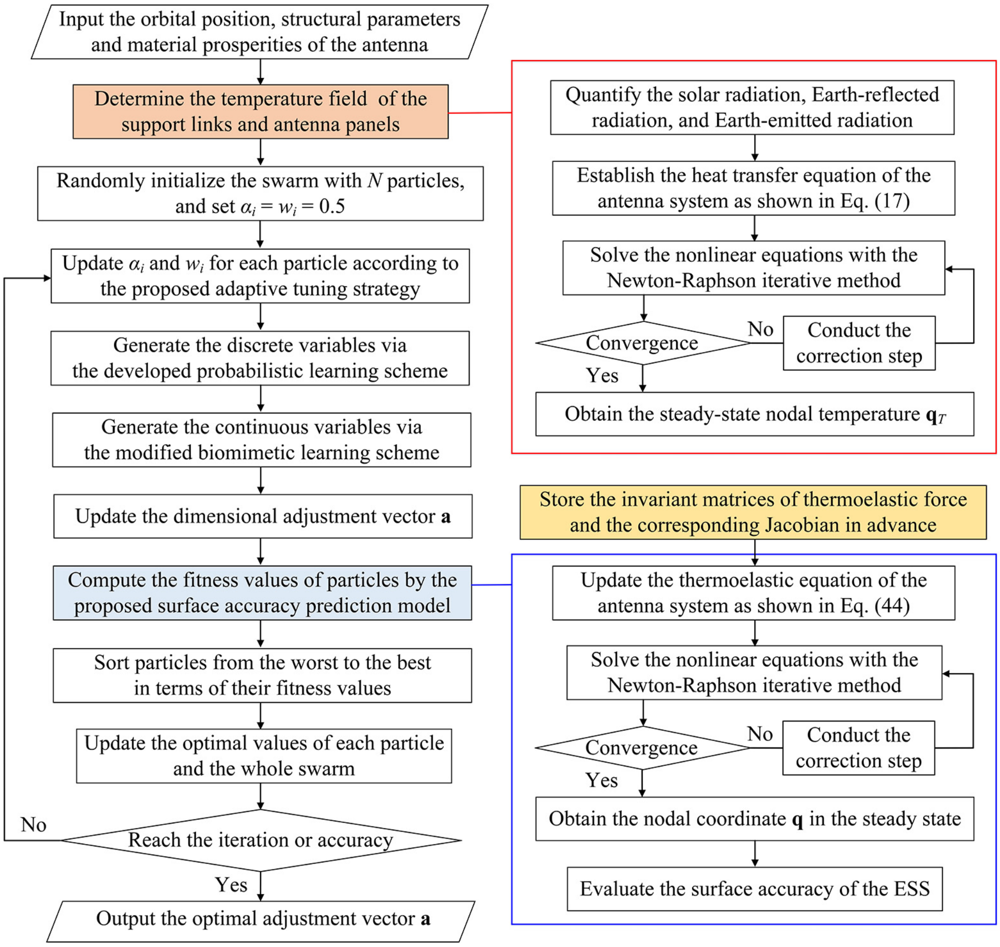

Fig. 8. The developed framework for the surface accuracy optimization.

Table 2
Thermoelastic characteristics of the antenna system.

Thermoelastic property	Support links		Antenna panels	
	Symbol	Value	Symbol	Value
Mass density [kg/m^3]	ρ_s	1.81×10^3	ρ_p	2.73×10^3
Elastic modulus [N/m^2]	E_s	8.40×10^{10}	E_p	7.17×10^{10}
Poisson's ratio	ν_s	0.307	ν_p	0.330
Specific heat [J/(kg K)]	c_s	952	c_p	880
Surface emissivity	ς_s	0.78	ς_p	0.95
Thermal radiation absorptivity	α_s	0.72	α_p	0.79
Thermal expansion coefficients [K^{-1}]	ϖ_s	4.8×10^{-5}	ϖ_x, ϖ_y	2.6×10^{-5}
Thermal conductivity coefficients [W/(m K)]	k_s	25.75	k_1, k_2, k_3	17.31

6.2. Verification of the surface accuracy prediction at ambient temperature

In order to lay a solid foundation for the active adjustment, the effectiveness and adaptability of the accuracy prediction model are first confirmed by the ground test under ambient temperature. As shown in Fig. 9, we utilize the laser tracker Leica TN90® to measure the surface deviation of the antenna panels. To simulate the dimensional adjustment, the gaskets with different thicknesses are to be placed into the interfaces between the support links and revolute joints.

In the benchmark experiment, the surface accuracy of the antenna is first measured at the reference temperature without taking into account any dimensional deviations of support links. Attributed to the ultra-precision machining, the initialized RMS deviation is only 0.0047 mm, indicating that the initialized deviation is negligible compared to the thermally induced deformation.

Under different ambient temperatures and dimensional deviations, three illustrative cases as presented in Table 3 are investigated to shed light on the verification. Computationally, each support link is separated into 8-12 beam elements, and each antenna panel is divided into 416 thin plate elements. Given the temperature field and the dimensional deviations, the thermoelastic deformations of antenna panels in the three cases are solved and depicted in Fig. 10.

It can be observed that the antenna panels may suffer from different strain patterns, with more stress concentrated at the edges of the outer panel. The maximum deformations in the three cases are 8.1896 mm, 6.2985 mm, and 13.549 mm, respectively. With reference to the panel thickness, the thermoelastic deformation is serious enough to affect the antenna's electric performance.

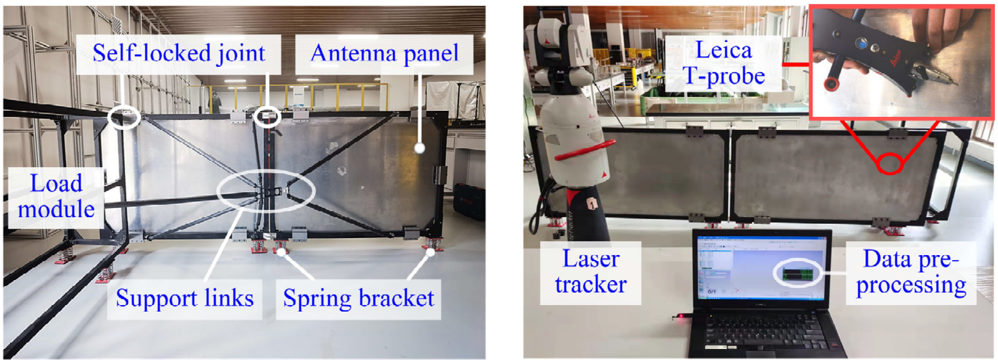

(a) Support links and antenna panels

(b) Surface accuracy measurement

Fig. 9. Experiment and measurement system.

Table 3
Dimensional adjustment and temperature difference in the experiment.

Case	Δl_0 /mm	Δl_1 /mm	Δl_2 /mm	Δl_3 /mm	Δl_4 /mm	Δl_5 /mm	Δl_6 /mm	ΔT /°C
No. 1	−1.62	1.18	1.66	−1.56	0.24	−2.32	−1.70	10
No. 2	0.58	1.96	−0.84	1.62	−1.34	−1.50	1.82	15
No. 3	2.94	−0.32	−1.16	1.04	−0.58	1.78	2.06	20

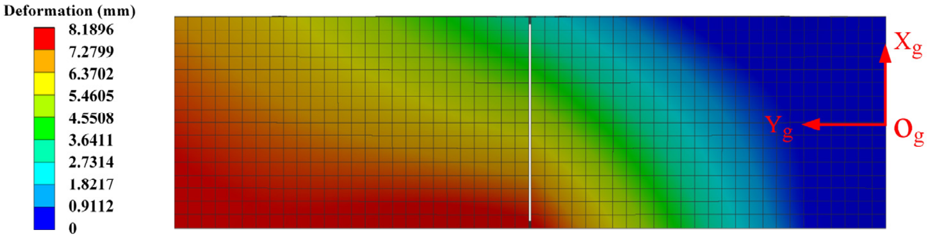

(a) Case 1

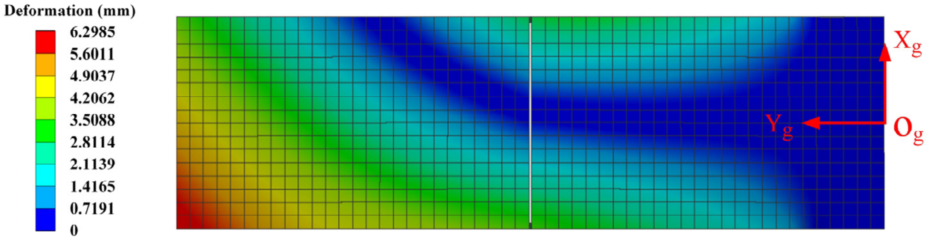

(b) Case 2

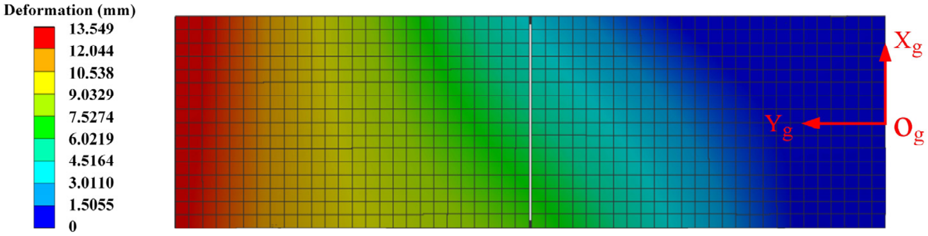

(c) Case 3

Fig. 10. Thermoelastic deformation of antenna panels at ambient temperature.

Table 4 displays the antenna surface accuracy obtained from the prediction and experiment. The comparison results show that the absolute maximum RMS deviation is only 2.48%. More vividly, the position coordinates of antenna panels after thermoelastic deformation are shown in Fig. 11, where the actual measurement points almost overlap with the predicted plane. These slight differences reflect that the proposed thermal-structural model is capable of predicting the antenna surface accuracy with satisfactory performance.

To further verify the feasibility of the developed method, three experiments are carried out separately under different temperatures and dimensional deviations. For this purpose, all dimensional deviations are initialized to zero, and then the support links are adjusted to compensate for the accuracy deviation caused by the temperature variation. The iteration process of the developed optimization algorithm for the three cases is depicted in Fig. 12. It is observed that stable convergence solutions can be achieved after 34 itera-

Table 4
Surface accuracy comparison of predictions and experiments.

Case	Predicted RMS deviation /mm	Experimental RMS deviation /mm	Relative error
No. 1	5.1774	5.3092	−2.48%
No. 2	2.4301	2.4157	0.59%
No. 3	7.1623	7.0735	1.26%

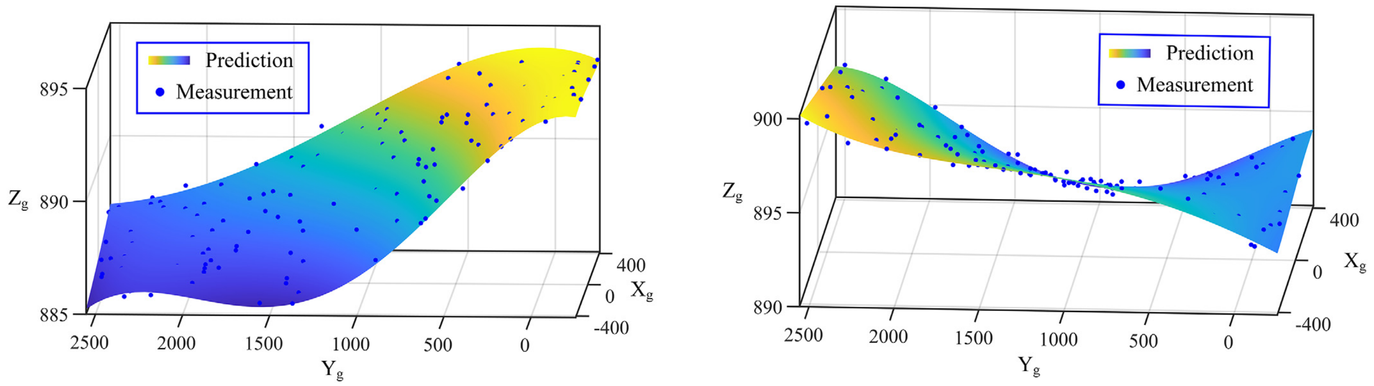

(a) Case 1 (b) Case 2

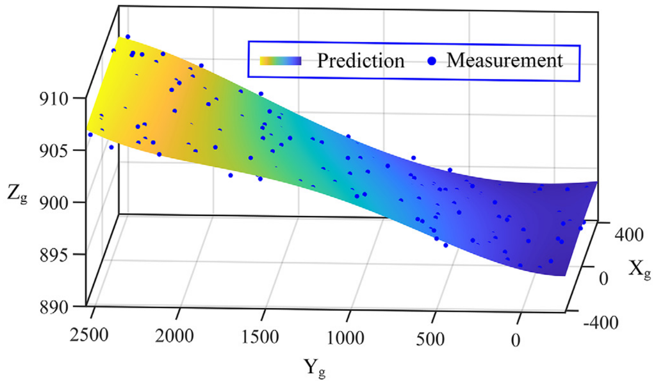

(c) Case 3

Fig. 11. Fitting plane of antenna panels from experiment and prediction.

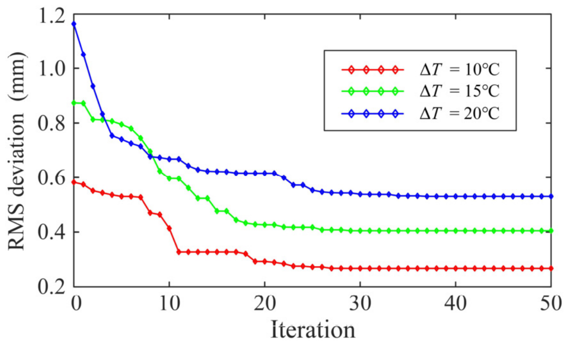

Fig. 12. Iterative optimization of the RMS deviations.

tions. Consequently, the adjustment vectors are determined as [−0.5693, −0.5654, −0.5654, −0.1857, −0.1857, −0.0472, −0.0472] mm, [−0.8018, −0.8764, −0.8764, −0.3573, −0.3573, −0.0664, −0.0664] mm, and [−1.2846, −1.2412, −1.2412, −0.4339, −0.4339, 0.0935, 0.0935] mm, respectively. Table 5 compares the corresponding theoretical and experimental results with and without link adjustment. The minor relative errors affirm the high accuracy of the established thermoelastic model for predicting the surface deviation of antenna panels. Moreover, the RMS deviations with link adjustment reduce by 51.96%, 54.64%, and 52.93% in the three cases, respectively. These results demonstrate the effectiveness of the developed optimization algorithm in regulating surface accuracy.

The above experimental studies have demonstrated the high accuracy and reliability of the developed thermoelastic model and optimization framework under the ambient temperature condition. From a purely mathematical perspective, we can deduce that the methods are generally valid for any temperature since we did not introduce any assumptions regarding the temperature condition. In other words,

Table 5
Surface accuracy compensation in the ground experiments.

Case	ΔT /°C	Initial RMS deviation /mm			Optimized RMS deviation /mm		
		Predicted	Experimental	Relative error	Predicted	Experimental	Relative error
No. 1	10	0.5820	0.5862	−0.72%	0.2674	0.2816	−5.04%
No. 2	15	0.8735	0.9124	−4.26%	0.4048	0.4139	−2.20%
No. 3	20	1.1641	1.1487	1.34%	0.5302	0.5407	−1.94%

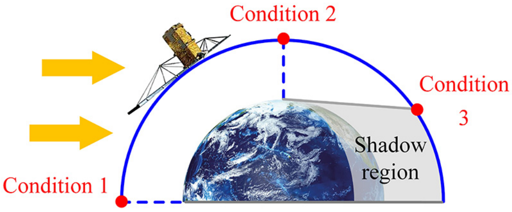

Fig. 13. Working conditions for the surface accuracy optimization.

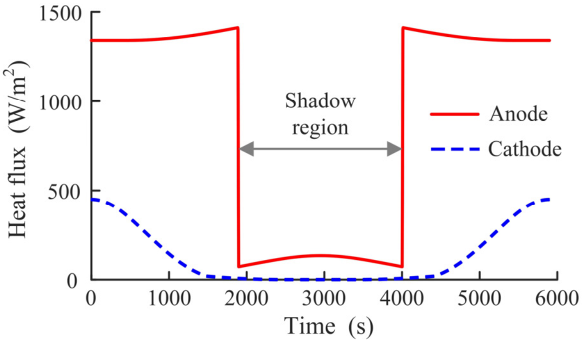

Fig. 14. The total heat flux subjected to the antenna.

changing the ambient temperature will not affect the applicability of the methods. Therefore, we will employ the developed methods to study the antenna systems under on-orbit temperature conditions.

6.3. Surface accuracy optimization for the antenna on orbit

After verifying the prediction accuracy of the thermoelastic model, we conduct the on-orbit active adjustment for optimizing the antenna surface accuracy. For demonstration, three indicative working conditions as shown in Fig. 13 are elucidated to adjust the thermally induced deformation.

The satellite altitude is 685 km, and the orbital period is 98.31 min. The outer space is considered a black body with an average temperature of 2.73 K. The reference temperature of the antenna is initialized as 294.25 K. Based on the formulation in Section 3.1, the total heat flux subjected to the antenna is determined and quantified as shown in Fig. 14.

According to the developed heat transfer model, the temperature field of two panels is depicted in Fig. 15. Due to the structural symmetry, the temperature distributions are also symmetric with respect to the Y_g axis. In particular, the uneven temperature field indicates the uniform assumption in previous studies is impractical. By contrasting the first and third conditions, it can be found that the temperature difference is as high as 182.51 K.

Moreover, the corresponding FE model is built through the commercial software ANSYS, and the temperature differences of both support links and antenna panels are simulated. The analytic results are compared in Tables 6 and 7 in detail. Regarding the temperature differences of the support links, the maximum relative errors under the three conditions are 2.34%, 4.18%, and 0.82%, respectively. As to the temperature differences of antenna panels, the maximum relative errors between the prediction and simulation results are 1.40%, 4.02%, and 1.31%, respectively. Therefore, the established heat transfer model is capable of precisely calculating the temperature field of the on-orbit SAR antenna.

Once the temperature field is determined, the RMS deviation of the antenna can be solved and optimized as formulated in Sections 4 and 5. Fig. 16 shows the convergence process of the developed mixed-variable optimization algorithm. The antenna surface deviations under the three working conditions reach the minimum after 85, 91, and 59 iterations, respectively. As presented in Table 8, the active optimization adjustment decreases the initial RMS deviations by 83.61%, 86.82%, and 74.80%, respectively. Moreover, among the three conditions, the optimized maximum deformation of the antenna panels is less than 14.8002 mm.

On a laptop with an Intel Core i7-2.5 GHz processor, the developed optimization algorithm requires an average of 864.07 seconds to determine the adjustment vectors for the three conditions. In terms of practical application, two key points regarding on-orbit active adjustment are noteworthy. Firstly, active adjustment is infrequent considering the system reliability and energy consumption. Secondly, the orbits of such spaceborne antennas are typically stable, exhibiting periodic thermally induced deformations. Therefore, it is feasible to pre-calculate the adjustment vectors, and then conduct on-orbit adjustment remotely by readily accessing the dataset. In addition, the use of memory alloys would make the strategy more attractive, and parallel computing techniques can be employed to further improve the optimization efficiency.

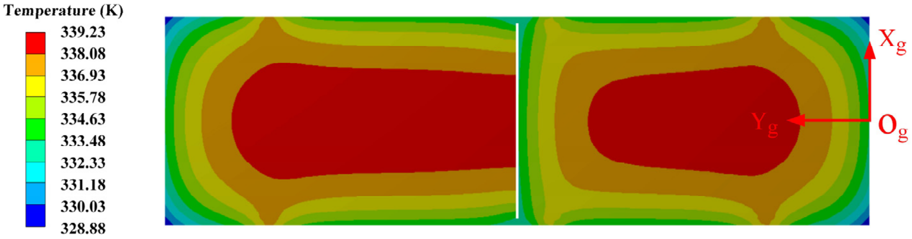

(a) Condition 1

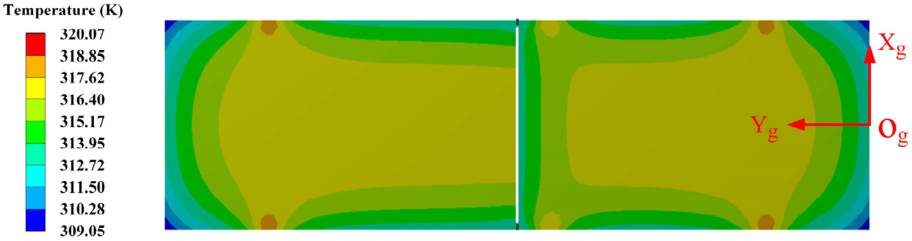

(b) Condition 2

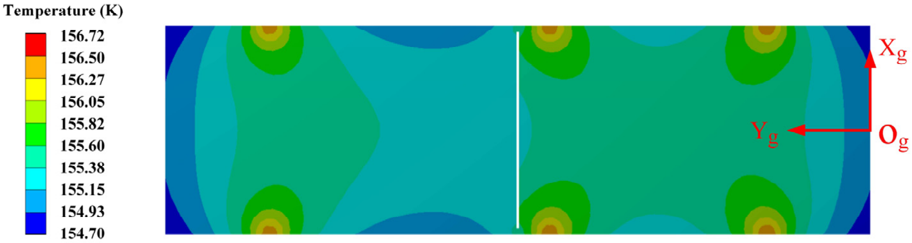

(c) Condition 3

Fig. 15. Temperature distribution of the antenna panels.

Table 6
Temperature differences of the support links (unit: K).

Condition	Temperature difference	ΔT_0	ΔT_1, ΔT_2	ΔT_3, ΔT_4	ΔT_5, ΔT_6
No. 1	Prediction	90.1081	77.0126	77.4337	78.0132
	Simulation	89.2158	77.1731	75.6599	77.2859
	Relative error	0.46%	−0.21%	2.34%	0.94%
No. 2	Prediction	89.8663	75.1676	74.5371	75.1414
	Simulation	89.0870	74.3253	71.5476	74.4623
	Relative error	−1.37%	1.13%	4.18%	0.91%
No. 3	Prediction	−110.8710	−122.1178	−122.9239	−121.6940
	Simulation	−111.7893	−122.5535	−123.5429	−122.0141
	Relative error	−0.82%	−0.36%	−0.50%	−0.26%

Table 7
Temperature differences of the antenna panels (unit: K).

Condition	Temperature difference	ΔT_{p1}	ΔT_{p2}	ΔT_{p3}	ΔT_{p4}	ΔT_{p5}	ΔT_{p6}
No. 1	Prediction	39.1544	44.4609	39.2576	44.5162	44.5709	39.2111
	Simulation	38.7192	45.6731	39.8137	44.0225	44.8376	38.7219
	Relative error	1.12%	−2.65%	−1.40%	1.12%	−0.59%	1.26%
No. 2	Prediction	18.5683	23.2103	18.9164	23.0981	23.2232	18.5641
	Simulation	18.1476	22.8167	19.3863	23.8850	23.0362	17.8470
	Relative error	2.32%	1.73%	−2.42%	−3.29%	0.81%	4.02%
No. 3	Prediction	−139.2725	−138.7118	−138.9536	−138.9237	−138.8102	−139.2921
	Simulation	−139.8940	−138.0724	−137.2381	−137.6314	−137.0217	−138.3089
	Relative error	−0.44%	0.46%	1.25%	0.94%	1.31%	0.71%

6.4. Further discussion

In practical engineering, not all the support links are always available to be adjusted because of the limitation of energy consumption. Therefore, it is worth discussing how the number of optional links affects the surface accuracy optimization of the spaceborne antenna. For this purpose, the dimensional adjustments with 1-4 links are demonstrated here in detail under the first working condition. As revealed in Table 9, the RMS deviation and the maximum deformation become larger with the increasing number of adjustable links. Nevertheless,

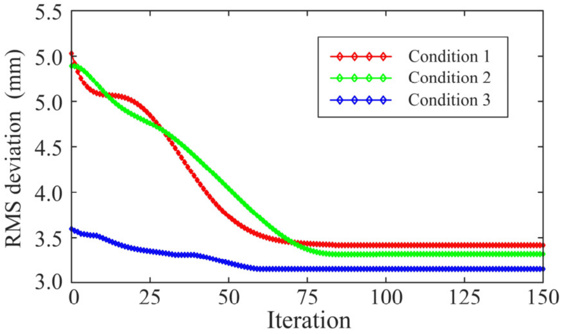

Fig. 16. Convergence process of the developed optimization algorithm.

Table 8
Surface accuracy optimization results with complete adjustment (unit: mm).

Condition	Initial RMS deviation	Optimized RMS deviation	Dimensional adjustment vector
No. 1	5.0572	0.8290	[−2.72, 0.13, −0.10, 1.32, 0.91, −0.85, 1.06]
No. 2	4.7849	0.6304	[−3.08, −3.24, −3.24, 1.86, 1.20, −2.26, −1.85]
No. 3	1.1847	0.2985	[2.52, 0.54, 1.53, −0.38, 0.02, −3.15, −2.59]

Table 9
Surface accuracy optimization results with partial adjustment (unit: mm).

N_a	Optimized RMS deviation	Optimized maximum deformation	Dimensional adjustment vector
4	1.3569	14.5974	[0, 1.1518, 1.1486, 0, 0, −1.7670, −1.0144]
3	1.8104	16.3326	[−1.2897, 0.1441, 0, 0, 0, −1.4262, 0]
2	2.7306	20.2891	[0, 1.2062, 1.0668, 0, 0, 0, 0]
1	3.6172	23.5549	[−1.4057, 0, 0, 0, 0, 0, 0]

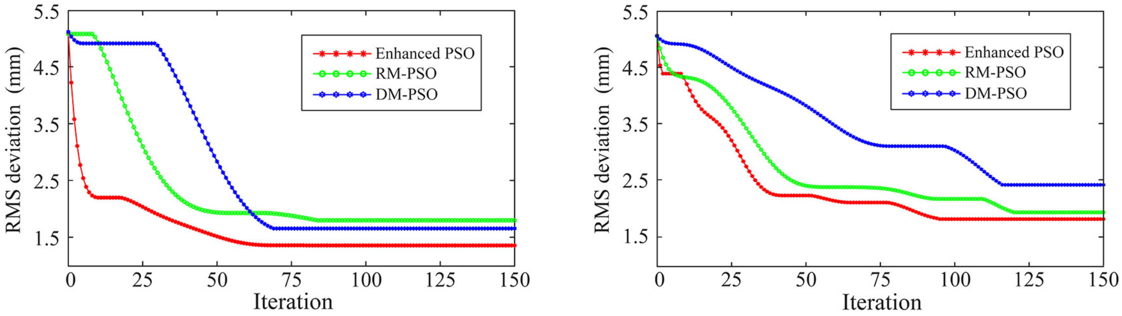

(a) Dimensional adjustment with 4 links

(b) Dimensional adjustment with 3 links

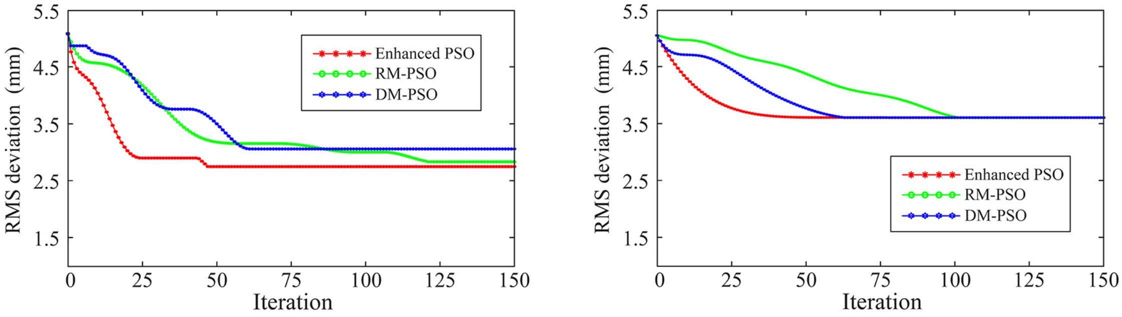

(c) Dimensional adjustment with 2 links

(d) Dimensional adjustment with 1 link

Fig. 17. Convergence curves of different optimization algorithms.

the desired surface accuracy can be obtained simply by altering the length of three support links, i.e., the partial adjustment also has great potential to compensate for the thermally induced deformation of antenna panels very well.

As shown in Table 9, the optimal adjustment positions can disrupt the structural symmetry due to the non-uniform temperature field. For instance, when there are 3 links to be adjusted, the optimal choice is the auxiliary link (l_0), the internal link (l_1), and the external link (l_5). However, if the optional links are even in number, it is advisable to prioritize the internal links. In addition, it is noteworthy that the partial adjustment with different links corresponds to different adjustment positions, and none of the links exhibits a clear advantage in compensating for the surface accuracy.

Furthermore, the developed multi-variable optimization algorithm is compared with the relaxation method (RM) [64] and the discretization method (DM) [27], which are also incorporated into the PSO framework. The corresponding convergence curves are depicted in Fig. 17. The presence of multiple constraints can produce large infeasible regions in the search space, causing the RM and DM to get trapped in local optima. Besides, the RM relies on a simple round mechanism to update the discrete variables, which inevitably yields suboptimal solutions and reduces convergence efficiency. The DM divides the whole search space into discrete segments without distinction and requires longer binary-coded strings, resulting in slower convergence. By leveraging separate reproduction schemes for continuous and discrete variables, the enhanced optimization framework outperforms the other two methods in terms of optimal value and convergence speed. Consequently, the proposed mixed-variable optimization algorithm is more efficient for the active dimensional adjustment.

7. Conclusions

This article has proposed and demonstrated an active optimization adjustment method for the surface accuracy control of spaceborne SAR antennas. Instead of simply assuming the even temperature distribution of the whole antenna system, the heat transfer model under the complex spatial thermal fluxes has been established to determine the specific temperature field. Afterward, considering the thermoelastic effect and the geometrical nonlinearity, the surface accuracy prediction model has been developed for evaluating the structural deformation in the service environment. Moreover, the thermoelastic force and its Jacobian matrix have also been explicitly derived with the technique of invariant matrices, which has improved the solving efficiency and accuracy of the thermal-structural response. After converting the thermoelastic deformation compensation into an objective optimization problem with multiple prescribed constraints, we have further proposed an enhanced mixed-variable optimization algorithm to obtain the superior active adjustment strategy. In particular, the proposed hybrid encoding scheme and the adaptive tuning approach have strengthened the diversity and convergence of the optimization algorithm, endowing an excellent performance in minimizing the antenna surface deviation. Finally, the case study has verified the feasibility and superiority of the proposed active optimization adjustment method.

In summary, our research not only proposes an effective theoretical prediction framework for the thermally induced deformation of the antenna system, but also extends the ground pre-adjustment to on-orbit active adjustment for surface accuracy compensation, facilitating the performance improvement of the spaceborne SAR antennas. Since this work focuses on establishing the surface accuracy adjustment framework of such antenna systems, the integrated structural-electromagnetic performance optimization [21] will be explored in further work.

Declaration of competing interest

The authors declare that they have no known competing financial interests or personal relationships that could have appeared to influence the work reported in this paper.

Data availability

No data was used for the research described in the article.

Acknowledgement

This study is supported by the National Natural Science Foundation of China (Grant No. 2022YFB3304200). The assistance from Feifei Chen is greatly appreciated, who is working as a senior engineer at the Shanghai Institute of Aerospace System Engineering.

References

[1] H. Kim, Y. Chang, Optimal mission scheduling for hybrid synthetic aperture radar satellite constellation based on weighting factors, Aerosp. Sci. Technol. 107 (2020) 106287.
[2] O. Kechagias-Stamatis, N. Aouf, Automatic target recognition on synthetic aperture radar imagery: a survey, IEEE Aerosp. Electron. Syst. Mag. 36 (2021) 56–81.
[3] P. Yuan, B. He, L. Zhang, R. Nie, X. Ma, Pretension modeling and form-finding for cable-network antennas with varying topologies and parameters, Aerosp. Sci. Technol. 112 (2021) 106631.
[4] M. Chandra, S. Kumar, S. Chattopadhyaya, S. Chatterjee, P. Kumar, A review on developments of deployable membrane-based reflector antennas, Adv. Space Res. 68 (2021) 3749–3764.
[5] W. Liu, D. Li, X. Yu, J. Jiang, Exact mesh shape design of large cable-network antenna reflectors with flexible ring truss supports, Acta Mech. Sin. 30 (2014) 198–205.
[6] R. Nie, B. He, S. Yan, X. Ma, Optimization design method for mesh reflector antennas considering the truss deformation and thermal effects, Eng. Struct. 208 (2020) 110253.
[7] D. Yu, Q. Zhao, J. Guo, F. Chen, J. Hong, Accuracy analysis of spatial overconstrained extendible support structures considering geometric errors, joint clearances and link flexibility, Aerosp. Sci. Technol. 119 (2021) 107098.
[8] J. Du, Y. Zong, H. Bao, Shape adjustment of cable mesh antennas using sequential quadratic programming, Aerosp. Sci. Technol. 30 (2013) 26–32.
[9] G. Xun, H. Peng, S. Wu, Z. Wu, Active shape adjustment of large cable-mesh reflectors using novel fast model predictive control, J. Aerosp. Eng. 31 (2018) 04018038.
[10] Q. Zhao, J. Guo, D. Yu, J. Hong, F. Chen, An enhanced method of resizing support links for a planar closed-loop overconstrained deployable structure considering kinematic reliability and surface accuracy, Aerosp. Sci. Technol. 104 (2020) 105988.
[11] D. Yu, J. Guo, T. Wu, J. Hong, Q. Zhao, Link adjustment for assembly deviation control of extendible support structures via sparse optimization, IEEE Access 9 (2021) 24060–24070.
[12] T.Y. Park, S.Y. Kim, D.W. Yi, H.Y. Jung, J.E. Lee, J.H. Yun, H.U. Oh, Thermal design and analysis of unfurlable CFRP skin-based parabolic reflector for spaceborne SAR antenna, Int. J. Aeronaut. Space Sci. 22 (2021) 433–444.
[13] E. Azadi, S.A. Fazelzadeh, M. Azadi, Thermally induced vibrations of smart solar panel in a low-orbit satellite, Adv. Space Res. 59 (2017) 1502–1513.
[14] A. Sharma, R. Kumar, R. Vaish, V.S. Chauhan, Active vibration control of space antenna reflector over wide temperature range, Compos. Struct. 128 (2015) 291–304.
[15] Z. Wang, T. Li, Y. Cao, Active shape adjustment of cable net structures with PZT actuators, Aerosp. Sci. Technol. 26 (2013) 160–168.
[16] X. Song, S. Tan, E. Wang, S. Wu, Z. Wu, Active shape control of an antenna reflector using piezoelectric actuators, J. Intell. Mater. Syst. Struct. 30 (2019) 2733–2747.
[17] A. Petosa, An overview of tuning techniques for frequency-agile antennas, IEEE Antennas Propag. Mag. 54 (2012) 271–296.
[18] S. Padula, H. Adelman, M. Bailey, R. Haftka, Integrated structural electromagnetic shape control of large space anatenna reflectors, AIAA J. 27 (1989) 814–819.
[19] J. Liu, L. Hollaway, Integrated structure-electromagnetic optimization of large reflector antenna systems, Struct. Optim. 16 (1998) 29–36.

[20] S. Zhang, B. Duan, Integrated structural-electromagnetic optimization of cable mesh reflectors considering pattern degradation for random structural errors, Struct. Multidiscip. Optim. 61 (2020) 1621–1635.
[21] S. Zhang, Z. Cao, S. Zhang, Form-finding design optimization method of cable mesh reflectors based on a weighting surface accuracy with electromagnetic performance, Struct. Multidiscip. Optim. 66 (2023) 1–17.
[22] S. Zhang, J. Du, B. Duan, G. Yang, Y. Ma, Integrated structural–electromagnetic shape control of cable mesh reflector antennas, AIAA J. 53 (2015) 1395–1399.
[23] H. Tanaka, Surface error estimation and correction of a space antenna based on antenna gainanalyses, Acta Astronaut. 68 (2011) 1062–1069.
[24] J. Mitsugi, T. Yasaka, K. Miura, Shape control of the tension truss antenna, AIAA J. 28 (1990) 316–322.
[25] M. Tabata, M. Natori, Active shape control of a deployable space antenna reflector, J. Intell. Mater. Syst. Struct. 7 (1996) 235–240.
[26] Z. Sun, B. Duan, Y. Zhang, D. Yang, N. Hu, Multi-material optimization design for mesh reflector antennas considering space thermal effects, Struct. Multidiscip. Optim. 65 (2022) 1–11.
[27] G. Lu, J. Zhou, G. Cai, G. Fang, L. Lv, F. Peng, Studies of thermal deformation and shape control of a space planar phased array antenna, Aerosp. Sci. Technol. 93 (2019).
[28] G. Yang, B. Duan, J. Du, Y. Zhang, Shape pre-adjustment of deployable mesh antennas considering space thermal loads, Proc. Inst. Mech. Eng., G J. Aerosp. Eng. 232 (2018) 143–155.
[29] R. Nie, B. He, S. Yan, X. Ma, Optimization design method for the cable network of mesh reflector antennas considering space thermal effects, Aerosp. Sci. Technol. 94 (2019) 105380.
[30] D. Yu, Y. Yang, G. Hu, Y. Zhou, J. Hong, Energy harvesting from thermally induced vibrations of antenna panels, Int. J. Mech. Sci. 231 (2022).
[31] Y. Cao, D. Cao, G. He, L. Liu, Thermal alternation induced vibration analysis of spacecraft with lateral solar arrays in orbit, Appl. Math. Model. 86 (2020) 166–184.
[32] S. Corpino, M. Caldera, F. Nichele, M. Masoero, N. Viola, Thermal design and analysis of a nanosatellite in low Earth orbit, Acta Astronaut. 115 (2015) 247–261.
[33] R. Kovács, V. Józsa, Thermal analysis of the SMOG-1 PocketQube satellite, Appl. Therm. Eng. 139 (2018) 506–513.
[34] M. Milman, W. Petrick, A note on the solution to a common thermal network problem encountered in heat-transfer analysis of spacecraft, Appl. Math. Model. 24 (2000) 861–879.
[35] Y. Liu, G. Li, L. Jiang, A new improved solution to thermal network problem in heat-transfer analysis of spacecraft, Aerosp. Sci. Technol. 14 (2010) 225–234.
[36] I. Torralbo, I. Perez-Grande, A. Sanz-Andres, J. Piqueras, Correlation of spacecraft thermal mathematical models to reference data, Acta Astronaut. 144 (2018) 305–319.
[37] J. Li, S. Yan, R. Cai, Thermal analysis of composite solar array subjected to space heat flux, Aerosp. Sci. Technol. 27 (2013) 84–94.
[38] E.Y. Maksimov, N. Yurkov, A. Yakimov, A finite-element model of the thermal influences on a microstrip antenna, Meas. Tech. 54 (2011) 207–212.
[39] W. Guo, Y. Li, Y.-Z. Li, S. Tian, S. Wang, Thermal–structural analysis of large deployable space antenna under extreme heat loads, J. Therm. Stresses 39 (2016) 887–905.
[40] D. Yu, Y. Yang, G. Hu, Y. Zhou, J. Hong, Energy harvesting from thermally induced vibrations of antenna panels, Int. J. Mech. Sci. 231 (2022) 107565.
[41] G.-Y. Lu, J.-Y. Zhou, G.-P. Cai, G.-Q. Fang, L.-L. Lv, F.-J. Peng, Studies of thermal deformation and shape control of a space planar phased array antenna, Aerosp. Sci. Technol. 93 (2019) 105311.
[42] K.N. Urata, J.T.S. Sumantyo, C.E. Santosa, T. Viscor, A compact C-Band CP-SAR microsatellite antenna for Earth Observation, Acta Astronaut. 159 (2019) 517–526.
[43] J. Liu, K. Pan, Rigid-flexible-thermal coupling dynamic formulation for satellite and plate multibody system, Aerosp. Sci. Technol. 52 (2016) 102–114.
[44] E. Sparrow, E. Niewerth, Radiating, convecting and conducting fins: numerical and linearized solutions, Int. J. Heat Mass Transf. 11 (1968) 377–379.
[45] X. Liu, G. Cai, Thermal analysis and rigid-flexible coupling dynamics of a satellite with membrane antenna, Int. J. Aerosp. Eng. 2022 (2022).
[46] C. Lee, J. Kim, Thermo-mechanical characteristics and stability boundaries of antenna structures in supersonic flows, Compos. Struct. 97 (2013) 363–369.
[47] X. Du, J. Du, H. Bao, G. Sun, Deployment analysis of deployable antennas considering cable net and truss flexibility, Aerosp. Sci. Technol. 82 (2018) 557–565.
[48] P. Li, C. Liu, Q. Tian, H. Hu, Y. Song, Dynamics of a deployable mesh reflector of satellite antenna: form-finding and modal analysis, J. Comput. Nonlinear Dyn. 11 (2016).
[49] C. Liu, Q. Tian, H. Hu, Dynamics of a large scale rigid–flexible multibody system composed of composite laminated plates, Multibody Syst. Dyn. 26 (2011) 283–305.
[50] A.A. Shabana, R.Y. Yakoub, Three dimensional absolute nodal coordinate formulation for beam elements: theory, J. Mech. Des. 123 (2001) 606–613.
[51] A.A. Shabana, An overview of the ANCF approach, justifications for its use, implementation issues, and future research directions, Multibody Syst. Dyn. (2023) 1–45.
[52] G. Wu, X. He, P.F. Pai, Geometrically exact 3D beam element for arbitrary large rigid-elastic deformation analysis of aerospace structures, Finite Elem. Anal. Des. 47 (2011) 402–412.
[53] K. Nachbagauer, P. Gruber, J. Gerstmayr, Structural and continuum mechanics approaches for a 3D shear deformable ANCF beam finite element: application to static and linearized dynamic examples, J. Comput. Nonlinear Dyn. 8 (2013).
[54] Y. Tang, Q. Tian, H. Hu, Efficient modeling and order reduction of new 3D beam elements with warping via absolute nodal coordinate formulation, Nonlinear Dyn. 109 (2022) 2319–2354.
[55] S. Kulkarni, A.A. Shabana, Spatial ANCF/CRBF beam elements, Acta Mech. 230 (2019) 929–952.
[56] K. Dufva, A.A. Shabana, Analysis of thin plate structures using the absolute nodal coordinate formulation, Proc. Inst. Mech. Eng., Proc., Part K, J. Multi-Body Dyn. 219 (2006) 345–355.
[57] G. Wang, H. Liu, Dynamics model of 4-SPS/CU parallel mechanism with spherical clearance joint and flexible moving platform, J. Tribol. 140 (2018) 021101.
[58] A. Borković, N. Mrđa, S. Kovačević, Dynamical analysis of stiffened plates using the compound strip method, Eng. Struct. 50 (2013) 56–67.
[59] D. Bratton, J. Kennedy, Defining a standard for particle swarm optimization, in: 2007 IEEE Swarm Intelligence Symposium, IEEE, 2007, pp. 120–127.
[60] F. Wang, H. Zhang, A. Zhou, A particle swarm optimization algorithm for mixed-variable optimization problems, Swarm Evol. Comput. 60 (2021).
[61] R. Poli, J. Kennedy, T. Blackwell, Particle swarm optimization, Swarm Intell. 1 (2007) 33–57.
[62] D. Wang, D. Tan, L. Liu, Particle swarm optimization algorithm: an overview, Soft Comput. 22 (2018) 387–408.
[63] A.R. Jordehi, A review on constraint handling strategies in particle swarm optimisation, Neural Comput. Appl. 26 (2015) 1265–1275.
[64] L. Gao, A. Hailu, Comprehensive learning particle swarm optimizer for constrained mixed-variable optimization problems, Int. J. Comput. Intell. Syst. 3 (2010) 832–842.